Microwave and submillimeter wave scattering of oriented ice particles

Manfred Brath[1], Robin Ekelund[2], Patrick Eriksson[2], Oliver Lemke[1], and Stefan A. Buehler[1]

[1]Universität Hamburg, Faculty of Mathematics, Informatics and Natural Sciences, Department of Earth Sciences, Meteorological Institute, Hamburg, Germany
[2]Department of Space, Earth and Environment, Chalmers University of Technology, Gothenburg, Sweden

Correspondence: Manfred Brath
(manfred.brath@uni-hamburg.de)

Abstract. Microwave dual-polarization measurements above 100 GHz are so far sparse, but they consistently show that larger ice hydrometeors tend to deviate from the standard assumption of total random orientation. This conclusion has been derived by conceptual models, while the first detailed simulations, recreating the observed polarization patterns, are presented in this study. The ice particles are assumed to be azimuthally randomly oriented with a fixed but arbitrary tilt angle. The scattering data for azimuthal random orientation is much more complex than for total random orientation. The scattering data of azimuthally randomly oriented particles depends in general on the incidence angle and two scattering angles compared to one angle scattering for total random orientation. The additional tilt angle adds an additional dimension. The simulations are based on the discrete dipol approximation in combination with a self developed orientation averaging approach. Data for two particle habits (51 hexagonal plates and 18 plate aggregates) and 35 frequencies between 1 GHz and 864 GHz were produced. The data is publicly available from Zenodo (https://doi.org/10.5281/zenodo.3463003). This effort is also an essential part of preparing for the upcoming Ice Cloud Imager (ICI), that will perform polarized observations at 243 GHz and 664 GHz, which will deliver new insights about clouds.

1 Introduction

Passive microwave (MW) observations are nowadays a standard tool for cloud observation. The ice cloud related sounding channels of these passive microwave sensors typically do not possess a fixed polarization or they measure only at one polarization. Observation of polarization in view of MW and submillimeter (SubMM) remote sensing of ice clouds is still rare. Currently, GMI (GPM (Global Precipitation Measurement) Microwave Imager, Hou et al., 2013) and MADRAS (Microwave Analysis and Detection of Rain and Atmospheric Structure, Defer et al., 2014) are the only spaceborne microwave radiometer that measure polarization at ice cloud related frequencies. GMI and MADRAS observe polarization around 160 GHz. With the upcoming ICI (Ice Cloud Imager, Eriksson et al. (2019); Bergadá et al. (2016); Buehler et al. (2012, 2007)) there will be polarized observations at 243 GHz and at 664 GHz. These polarized observations will deliver new insights about clouds and their structure, because the assumption of totally randomly oriented particles cannot explain the strong polarization signals found in

Defer et al. (2014); Gong and Wu (2017); Zeng et al. (2019). To understand these signals we need the scattering properties of realistically shape ice crystals that also possess an orientation.

25   Defer et al. (2014); Gong and Wu (2017) and Zeng et al. (2019) showed MW observations of polarized scattering signals of clouds using GMI and MADRAS. Defer et al. (2014) and Gong and Wu (2017) explained these polarized signals in conceptually using very simplified assumptions on shape and orientations. In reality, ice crystals have several shapes and sizes. Furthermore, even the cases that have been explained by horizontally aligned particles consist in reality not only of particles with only one orientations, but of particles with several different orientations, from which some orientations have a higher

30 probability than other orientations.

    Existing single scattering databases of frozen hydrometeors at microwave and submillimeter range like the ones of Eriksson et al. (2018), Liu (2008) or Hong et al. (2009) assume total random orientation of the scatterers, which is often a reasonable assumption, but cannot explain polarized cloud signals. The studies of Lu et al. (2016) and of Adams and Bettenhausen (2012) take orientation into account but are limited to frequencies below 94 GHz and 166 GHz, respectively.

35   The aim of this paper is to simulate the MW and SubMM scattering properties of realistically shaped ice crystals that are randomly oriented in azimuth but possess a fixed arbitrary tilt angle relative to zenith. The resulting single scattering database is publicly available from Zenodo (https://doi.org/10.5281/zenodo.3463003). The scattering database is structured so that it can be used together with the scattering database of Eriksson et al. (2018). The idea of our approach is to simulate the scattering of ice crystals from various incidence directions and then use these simulations for the orientation averages. Similar to the work

40 of Eriksson et al. (2018), Adams and Bettenhausen (2012), Hong et al. (2009) or Liu (2008) the scattering is simulated on the basis of the discrete dipole approximation (DDA, Draine and Flatau (1994)). Furthermore, the simulated scattering properties of azimuthally randomly oriented ice particles are used for radiative transfer simulations of cloudy scenes to investigate their influence on actual brightness temperature observations.

    The text is structured as follows: in Sect. 2 we explain the particle orientation. Sect. 3 provides an overview of the basic setup

45 and the simulated particles. Sect. 4 explains the scattering simulation. Sect. 5 shows some example results. Sect. 6 considers the influence of the simulated scattering properties in view of radiative transfer simulations. In Sect. 7 we summarize the results.

2   Particle orientation

Particle orientation refers to how the main axes of the particle are oriented with respect to the local horizon and the azimuthal reference. If the particle possesses spherical symmetry there is no particle orientation, because it does not matter from which

50 side the particle with spherical symmetry is viewed or how it is rotated - it will always look the same. As the particles considered in this paper do not have a spherical symmetry they have an orientation.

    In general, the orientation of a particle in a three dimensional space can be described by a set of three parameters. The three Euler angles are one such parameter set. The Euler angles define the orientation of the particle (coordinate) system relative to a fixed coordinate system, hereafter called laboratory system. The particle system is the coordinate system that is attached to the

55 particle. This means, if a particle is rotated, the particle system is rotated the same way. The laboratory system stays under the
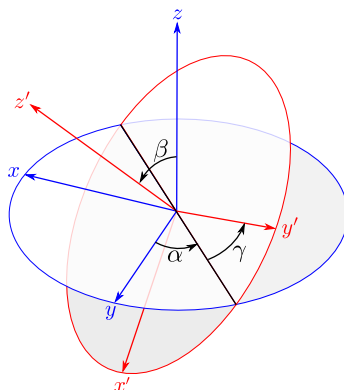
Figure 1. Euler angles

rotation of the particle whereas the particle system changes its orientation. The laboratory system and particle system share the same origin. In this study, the Euler angles, which are shown in Fig. 1, are used according to the z⊠z'-notation. The particle is first rotated by angle α around the laboratory Z-axis, then the particle is rotated by angle β around the particle Y-axis (⊠′) and last the particle is rotated by angle γ around the particle Z-axis. The value ranges of the angles are

$$\alpha \in [0, 2\pi]$$

60 $$\beta \in [0, \pi]$$ (1)

$$\gamma \in [0, 2\pi]$$

These rotations are described by three orthogonal rotation matrices, see Sect. 4.1 for details. It is important to know that the order of the rotation must not be changed, because the combination of rotations is not commutative.

Additionally to the Euler angles, the orientation of the non-rotated particle is needed. As there is no absolute coordinate system, the orientation of the non-rotated particle is in general arbitrary. Therefore, we define that the non-rotated particle

65 lies with its center of gravity at the origin of the laboratory system and all particle rotations will be relative to the origin of the laboratory system. The non-rotated particle is defined to have its principal moments of inertia axes aligned along the Cartesian coordinate axes, with the maximum inertia axis along the z-axis and the smallest along the x-axis (see Appendix A). This means for a plate-like particle that its longest dimensions lay parallel to the x-y-plane. This is the orientation that one intuitively expects for a falling plate-like particle in air.

70 Within this study, we are not interested in the scattering of a single oriented particle but in the scattering of an ensemble of oriented particles. Generally, the scattering properties of ensembles of oriented particles are described by averaging the single scattering properties over the three Euler angles, such that for example for the scattering matrix Z_{eo} and the extinction matrix K_{eo} of an ensemble of orientated particles hold

$$Z_{eo}(\theta_{inc}, \phi_{inc}, \theta_s, \phi_s) = \int\limits_0^{2\pi} \int\limits_0^{\pi} \int\limits_0^{2\pi} p_\alpha(\alpha) p_\beta(\beta) p_\gamma(\gamma) \, Z(\theta_{inc}, \phi_{inc}, \theta_s, \phi_s, \alpha, \beta, \gamma) \, \sin\beta \, d\alpha \, d\beta \, d\gamma \tag{2}$$

75

$$K_{eo} = (\theta_{inc}, \phi_{inc}) = \int_0^{2\pi} \int_0^{\pi} \int_0^{2\pi} p_\alpha(\alpha) p_\beta(\beta) p_\gamma(\gamma) \, K(\theta_{inc}, \phi_{inc}, \alpha, \beta, \gamma) \sin\beta \, \mathrm{d}\alpha \, \mathrm{d}\beta \, \mathrm{d}\gamma \tag{3}$$

with θ_{inc} the incidence polar angle, ϕ_{inc} the incidence azimuth angle, θ_s the scattering polar angle and ϕ_s the scattering azimuth angle. $p_j(x)$ are probability density functions describing the distribution of particle orientation. We distinguish between two basic states of particle orientation

80   1. total random orientation and

2. azimuthal random orientation.

Both orientation states are explained in the two following subsections.

2.1 Total random orientation

Totally randomly oriented particles are defined as the orientation average over the three Euler angles, in which the Euler angles

85 are uniformly distributed. That is,

$$p_\alpha(\alpha) = p_\gamma(\gamma) = \frac{1}{2\pi} \tag{4}$$

$$p_\beta(\beta) = \frac{1}{\pi}. \tag{5}$$

Due to this averaging, totally randomly oriented particles have effectively a spherical symmetry. This implies that the scattering matrix of totally randomly oriented particles depends only, like the scattering matrix of spheres, on the scattering angle Θ, i.e.

90 $Z_{\mathrm{tro}}(\Theta) = Z_{\mathrm{tro}}(\theta_{inc}, \phi_{inc}, \theta_s, \phi_s),$ \hfill (6)

and K_{tro} will have no angular dependency. The scattering angle Θ is the angle between incoming and outgoing direction. Eriksson et al. (2018), Ding et al. (2017), Liu (2008) and Hong et al. (2009) assume total random orientation in their databases.

2.2 Azimuthal random orientation

Azimuthally randomly oriented particles with a specific orientation to the horizon, also referred to as tilt or canting, are defined

95 as the orientation average over α and γ, in which α and γ are uniformly distributed as for total random orientation. The scattering matrix Z_{aro} and the extinction matrix K_{aro} of azimuthally randomly oriented particles are thus calculated as

$$Z_{\mathrm{aro}}(\theta_{inc}, \theta_s, \Delta\phi, \beta) = \int_0^{2\pi} \int_0^{2\pi} p_\alpha(\alpha) p_\gamma(\gamma) \, Z(\theta_{inc}, \phi_{inc}, \theta_s, \phi_s, \alpha, \beta, \gamma) \, \mathrm{d}\alpha \, \mathrm{d}\gamma \tag{7}$$
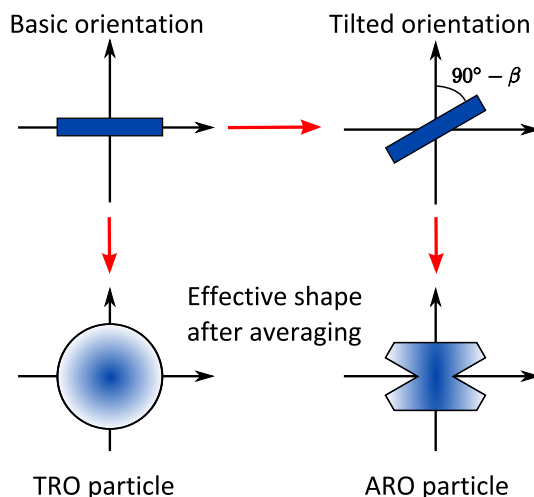
Figure 2. Schematic of the difference between totally random (TRO) and azimuthally random orientation (ARO).

$$\mathrm{K}_{\mathrm{aro}}(\theta_{inc}, \beta) = \int\limits_{0}^{2\pi} \int\limits_{0}^{2\pi} p_\alpha(\alpha) p_\gamma(\gamma) \, \mathrm{K}(\theta_{inc}, \phi_{inc}, \alpha, \beta, \gamma) \, \mathrm{d}\alpha \mathrm{d}\gamma \tag{8}$$

100 The averaging over α and γ results in a rotational symmetry of the scattering matrix to the laboratory Z-axis (cylindrical symmetry). The orientation average results in an effective particle shape as indicated in Fig. 2. To get a better picture of it, assume that the particle rotates very fast around the laboratory Z-axis and the particle Z-axis to symbolize the orientation averaging. By rotation it creates an effective solid of revolution. Changing the tilt angle β results in a different shape of this effective solid of revolution. Due to the cylindrical symmetry after orientation averaging, the averaged scattering matrix

105 depends in azimuth only on the difference between incident and scattered azimuth direction. Whereas the scattering matrix of totally randomly oriented particles depends only on the scattering angle Θ, the scattering matrix of azimuthally randomly oriented particles depends on the incidence polar angle θ_{inc}, the scattering polar angle θ_s, the difference of the incidence and scattering azimuth angles $\Delta\phi = \phi_{inc} - \phi_s$ and the tilt angle β. Without any loss of generality, the azimuth incidence angle ϕ_{inc} is set to 0° for the azimuthally randomly oriented case from here on. It is important to note that the azimuthal symmetry does

110 not mean that the scattering matrix $\mathrm{Z}_{\mathrm{aro}}$ is symmetric to incidence azimuth direction. This depends on the symmetry properties of the particles and the orientation of the rotation axes relative to the symmetry axes. To get a better idea of it, assume a flag rotates fast around its flagpole in counterclockwise direction. The flag has a white front side, a black backside and its hoist is to the left. Independent from which side we look on the flagpole, the projections of the white frontside are always seen on the right side of the flagpole and the projections of the black backside are always seen on the left side. If both sides of the flag have

115 the same color then the projections on both sides will look the same. Although the rotation results in a rotational symmetry around the flagpole, the actual image we see depends on the symmetry properties of the flag.

3 Basic setup and shape data

For the scattering calculations Amsterdam DDA (ADDA) version 1.2 was used. ADDA is a DDA implementation of Yurkin and Hoekstra (2011). The basic idea of DDA is to represent the particle by a discrete set of electric dipoles. For details of the DDA

120 method, see Yurkin and Hoekstra (2011) and the references therein. ADDA can simulate the scattering of totally randomly oriented particles and the scattering of particles with a fixed but arbitrary orientation. The internal averaging method of ADDA cannot be used for azimuthally oriented particles. Instead, we developed an averaging approach that involves integration over a set of DDA calculations at different angles, and transformations of reference frames, which is explained in Sect. 4.

In this work we consider two different types of frozen hydrometeor habits:

125 – plate type 1, which is a solid hexagonal plate-like single crystal, and

– large plate aggregate, which consists of several solid hexagonal plates aggregated to one particle.

The shape data including the actual dipole grids for ADDA were taken from the database of Eriksson et al. (2018). Following Eriksson et al. (2018), a habit is defined as a set of particles of different sizes, roughly following a mass-size relationship. The mass-size relationship is defined as

130 $$m = a \left(\frac{D}{D_0} \right)^b \tag{9}$$

with m the particle mass, D the maximum diameter, D_0 the unit diameter and the parameters a, b. Table 1 shows for each habit the size range and the values of the parameters a, b. Fig. 3 shows some different sized particles of both habits as example. For the plate type 1 habit, 51 differently sized particles were simulated. The size range is between $10\,\mu m$ and $2,596\,\mu m$ volume equivalent diameter, which corresponds to maximum diameters between $13\,\mu m$ and $10,000\,\mu m$. The plate type 1 habit in our

135 study has slightly different sizes than the plate type 1 in Eriksson et al. (2018). For the large plate aggregate habit, 18 differently sized particles were simulated. The size range is between $197\,\mu m$ and $4,563\,\mu m$ volume equivalent diameter, which corresponds to maximum diameters between $349\,\mu m$ and $22,860\,\mu m$. For details on the particle shape data the reader is referred to Eriksson et al. (2018).

In this work we follow the approach of Eriksson et al. (2018) for the temperature and frequency selection. The selected

140 frequency range of the scattering calculation consists of 35 frequencies between $1\,GHz$ and $864\,GHz$. Most selected frequencies are organized to include channel sets of existing and planned submillimeter and microwave radiometers. Table 2 shows the selected frequencies. The frequencies of the plate type 1 habit slightly deviate from the frequencies of the large plate aggregate habit by at maximum $0.5\,GHz$. The selected temperatures are $190\,K$, $230\,K$, and $270\,K$. Following Eriksson et al. (2018), the refractive index of ice is calculated by the model of Mätzler (2006).

Table 1. Overview of the selected habits. a- and b- are the parameters of the mass-size relationship (Eq. 9), D_{veq} is the volume equivalent diameter and D_{max} is the maximum diameter. ID is the identification number from the database of Eriksson et al. (2018).

habit name	ID	type	a [kg]	b	No. of sizes	D_{veq} [µm]	D_{max} [µm]
plate type 1	9	single crystal	0.76	2.48	51	$10 - 2,596$	$13 - 10,000$
large plate aggregate	20	aggregate	0.21	2.26	18	$197 - 4,563$	$349 - 22,860$
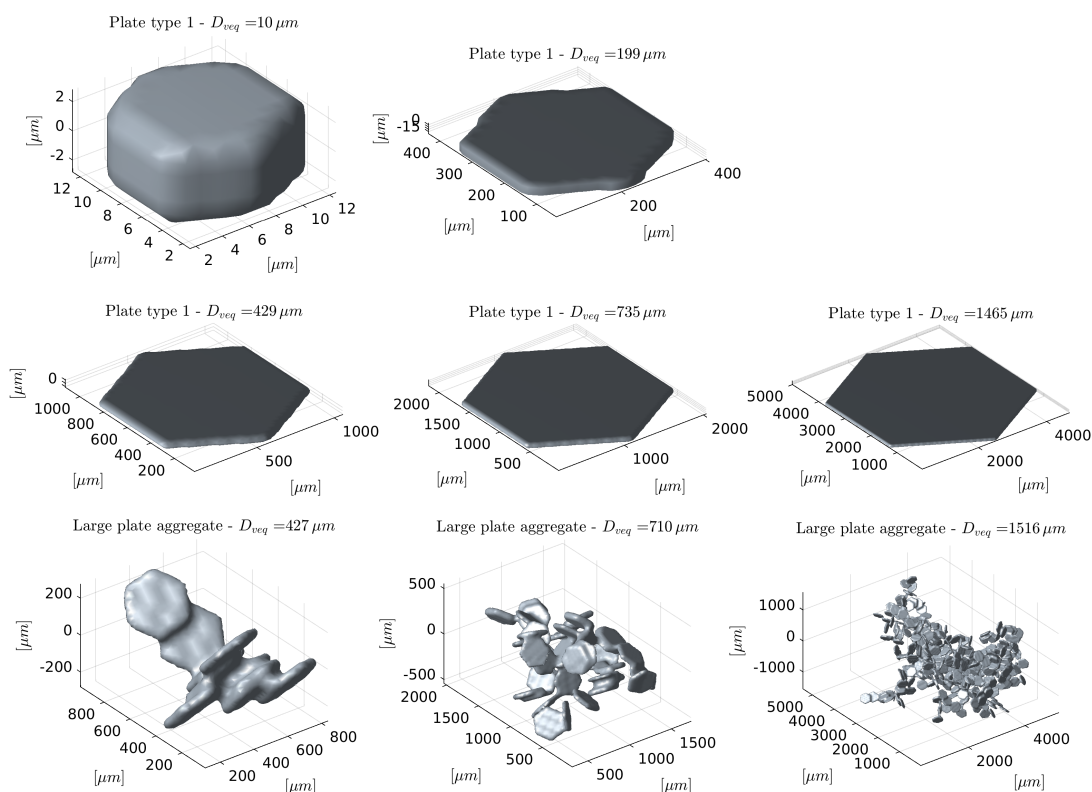
Figure 3. Example scatterer shapes.

Table 2. The frequencies for the scattering calculations. Except for $35.6\,\mathrm{GHz}$, the channels $\geq 18.6\,\mathrm{GHz}$ are organized in channel sets, see text.

Channel set	1	2	3	4	5	6	7	8	9	10	11	12
Freq.	18.6	31.3	50.1	88.8	115.3	164.1	175.3	228	314.2	439.3	657.3	862.4
[GHz]	24	31.5	57.6	94.1	122.2	166.9	191.3	247.2	336.1	456.7	670.7	886.4

Other frequencies [GHz]:

1, 1.4, 3, 5, 7, 9, 10, 10.65, 13.4, 15, 35.6
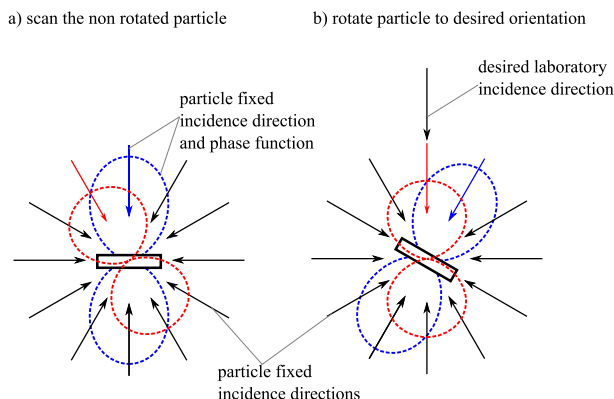
Figure 4. Schematic drawing of the calculation of the single scattering properties. (left) the non rotated particle with the incidence and scattering directions fixed to the particle. (right) the rotated particle and the rotated incidence and scattering directions.

4 Scattering calculations

In general, the scattering matrix Z of a non-spherical particle depends on the incidence direction $(\theta_{inc}, \phi_{inc})$, the scattering direction (θ_s, ϕ_s) and the particle orientation described by the three Euler angles α, β and γ. The same holds for the extinction matrix K except that it is independent of the scattering directions. The rotation of a particle is equivalent to the inverse rotation of the incidence direction. This means, it is equivalent if the scattering of a particle is calculated for any incidence angle at a fixed orientation or if the scattering of a particle is calculated for any orientation but at a fixed incidence angle. This equivalence is the key point in our approach. Therefore the scattering is calculated for any incidence direction and scattering direction and the particle orientation is kept fixed. The orientation averaging is calculated by rotating the incidence and scattering direction according to the particle orientation. With ADDA it is only possible to calculate the scattering properties for a finite set of incidence and scattering directions. So, the scattering matrix and the extinction matrix are calculated for a set of different incidence directions and scattering directions (only scattering matrix). The result is the scattering matrix and the extinction matrix for finite set of incidence and scattering directions, which are fixed to the particle, see Fig. 4a. For a specific orientation of the particle, the set of incidence and scattering directions are rotated accordingly to the orientation of the particle, see Fig. 4 b. This approach is analogue to the analytic T-matrix method, only in a much more numerical way.

The actual results of an ADDA calculation are the scattering amplitude matrix and the Mueller matrix for a desired incidence direction and a grid of scattering directions, whereas we are interested in extinction matrix and scattering matrix. The extinction matrix K depends on the scattering amplitude matrix for the forward direction ($\theta_{inc} = \theta_s$, $\phi_{inc} = \phi_s$, Mishchenko et al. 2002)

$$
K = \frac{2\pi}{k} \begin{pmatrix}
\mathrm{Im}(S_{11} + S_{22}) & \mathrm{Im}(S_{11} - S_{22}) & -\mathrm{Im}(S_{12} + S_{21}) & \mathrm{Re}(S_{21} - S_{12}) \\
\mathrm{Im}(S_{11} - S_{22}) & \mathrm{Im}(S_{11} + S_{22}) & \mathrm{Im}(S_{21} - S_{12}) & -\mathrm{Re}(S_{12} + S_{21}) \\
-\mathrm{Im}(S_{12} + S_{21}) & -\mathrm{Im}(S_{21} - S_{12}) & \mathrm{Im}(S_{11} + S_{22}) & \mathrm{Re}(S_{22} - S_{11}) \\
\mathrm{Re}(S_{21} - S_{12}) & \mathrm{Re}(S_{12} + S_{21}) & -\mathrm{Re}(S_{22} - S_{11}) & \mathrm{Im}(S_{11} + S_{22})
\end{pmatrix}
\tag{10}
$$

with the scattering amplitude matrix

$$S = \begin{pmatrix} S_{11} & S_{12} \\ S_{21} & S_{22} \end{pmatrix} = \frac{1}{-ik} \begin{pmatrix} s_2 & s_3 \\ s_4 & s_1 \end{pmatrix},$$ (11)

165 k the angular wave number and s_j the scattering amplitude matrix element of ADDA. Between the scattering matrix Z and the Mueller matrix M, which are both 4×4 matrices, following linear relationship holds

$$Z = \frac{1}{k^2} L_s M L_i$$ (12)

with L_i, L_s the stokes rotation matrices (Mishchenko et al., 2002). The stokes rotation matrices $L_{i,s}$ are defined in Sect. 4.2. Due to the linear relationship, it does not matter if first the Mueller matrix is transformed to a scattering matrix and then the

170 scattering matrix is averaged or vice versa. Instead of transforming every calculated Mueller matrix into the scattering matrix, the averaging will be done for the Mueller matrix and at the end the averaged Mueller matrix is transformed to the scattering matrix, which is described in Sect. 4.2.

Each Mueller matrix element $M_{ij}\left(\theta_{inc}, \phi_{inc}, \theta'_s, \phi'_s\right)$, which has a scattering direction grid spacing of 1°, is expanded as a spherical harmonics series over the scattering directions θ'_s, ϕ'_s (see Appendix D) to efficiently store the results of the ADDA

175 calculation. The prime denotes that the angles are related to the incidence direction and not to the laboratory system as the unprimed angles. The spherical harmonic series is truncated to the number of coefficients, for which the mean square error between the series expansion and the original representation is less than 0.5% of the standard deviation of the M_{11} element over the scattered direction.

For each incidence direction, ADDA automatically calculates the Mueller matrix for a desired regular grid of polar angles

180 and azimuth angles. A regular grid of polar and azimuth angles has the property that the grid spacing at the pole is much finer than at the equator. Actually, this is advantageous for scattering, because due to the definition of the Mueller matrix the forward peak and the backward peak are located at the poles.

For the set of incidence angles, a regular grid of polar angles and azimuth angles are disadvantageous, because for the incidence angle an isotropic sampling is needed but the distribution of the directions of a regular grid of polar angles and

185 azimuth angles is not isotropic. Therefore, an icosahedral grid is used, which is shown in Fig. 5. An icosahedral grid is almost isotropic. The distances between two neighboring vertices (grid points) is everywhere the same and an icosahedral grid consist of equilateral triangles, which have all the same size. This makes the icosahedral grid convenient for grid refinement and adjusting the grid size for the needed accuracy. An icosahedral grid can be set up by recursively bisecting the edges of an icosahedron and projecting the new vertices on a sphere. Such an icosahedral grid consists of

190 $$N_v = 10 \cdot (2l)^2 + 2$$ (13)

vertices and

$$N_t = 20 \cdot (2l)^2$$ (14)
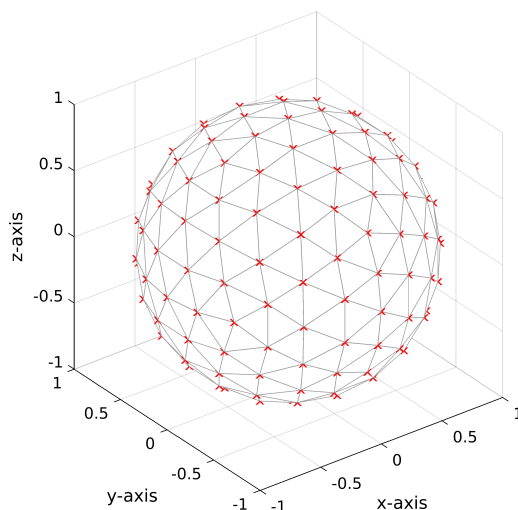
Figure 5. Example of an icosphere grid with 162 vertices. Each gridpoint represent an incoming angle for which a DDA calculation is preformed. This type of configuration ensures that the grid density is isotropic, making the overall calculations more efficient (a standard polar grid would be inefficient since it yields an excessive amount of angles around the 'North and South poles").

triangles with l the refinement level. The coordinates of the vertices of the icosahedral grid on the unit sphere are the set incidence directions. For more details on icosahedral grids, see for example Satoh (2014). For the scattering calculations

195   between 162 and 2562 incidence angles were used depending on the particle size and shape.

The actual orientation averaging is done by approximating

$$\mathrm{M}_{aro}\left(\theta_{inc}, \theta'_s, \phi'_s, \beta\right) = \int\limits_0^{2\pi} \int\limits_0^{2\pi} p_\alpha\left(\alpha\right) p_\gamma\left(\gamma\right) R^*_{\alpha\beta\gamma}\left(\mathrm{M}\right) \mathrm{d}\alpha \mathrm{d}\gamma \tag{15}$$

and

$$\mathrm{K}_{aro}\left(\theta_{inc}, \beta\right) = \int\limits_0^{2\pi} \int\limits_0^{2\pi} p_\alpha\left(\alpha\right) p_\gamma\left(\gamma\right) R^*_{\alpha\beta\gamma}\left(\mathrm{K}\right) \mathrm{d}\alpha \mathrm{d}\gamma \tag{16}$$

200   with a twofold with Gauss-Legendre quadrature. The rotation operator $R^*_{\alpha\beta\gamma}$ rotates the Mueller and the extinction matrix according to the desired orientation, which is explained in Sect. 4.1. The needed interpolation is done by using a barycentric interpolation for triangles, which is explained in appendix B. Afterwards the averaged Mueller matrix $\mathrm{M}_{aro}\left(\theta_{inc}, \theta'_s, \phi'_s, \beta\right)$ is transformed into the scattering matrix Z_{aro} using Eq. 12, which is explained in Sect. 4.2. As mentioned in Sect. 2.2, the resulting scattering matrix Z_{aro} is in general not symmetric to the incidence angle, as this depends on the actual particle. The

205   scattering matrix Z_{aro} is symmetric if it is averaged with its own mirrored version, in which it is reflected relative to the plane of incidence direction and laboratory Z-axis. This is equivalent to having simulated the scattering of the desired particle and its mirrored version, in which it is reflected by a plane that includes the laboratory Z-axis.

The methodology to calculate the scattering matrix and the extinction matrix can be summarized as:

1. DDA calculations: A set of DDA runs are performed over an icosahedral angle grid of incidence directions, demonstrated in Fig. 5. This type of grid ensures that the angle density is isotropic and increases the efficiency.

2. Averaging: Azimuthally averaged Mueller matrices $M_{aro}(\theta_{inc}, \theta'_s, \phi'_s, \beta)$ and extinction matrices $K_{aro}(\theta_{inc}, \beta)$ for a set of tilt angles β and polar incidence angles θ_{inc} are calculated by integrating the Mueller and extinction matrices over the Euler angles α and γ.

3. Transformation: The averaged Mueller matrices are transformed to averaged scattering matrices Z_{aro}.

4.1 Particle rotation

The key point in our averaging approach is the rotation of the particle for the averaging process. When rotating the particle the incidence and scattering direction change. The changed direction $\hat{e}_{i,rot}$ for a desired orientation is given by

$$\hat{e}_{i,rot} = R_{\alpha\beta\gamma}\hat{e}_i \tag{17}$$

with $\hat{e}_i$ the non-rotated incidence or scattering direction and $R_{\alpha\beta\gamma}$ the rotation matrix. The rotation matrix $R_{\alpha\beta\gamma}$ is

$$R_{\alpha\beta\gamma} = R(\alpha)R(\beta)R(\gamma) = \begin{pmatrix} R_{11} & R_{12} & R_{13} \\ R_{21} & R_{22} & R_{23} \\ R_{31} & R_{32} & R_{33} \end{pmatrix} \tag{18}$$

with the Euler angles α, β, and γ. See Appendix D for the rotation matrix elements R_{ij}. When the incidence and scattering directions change, the polarization directions change, too. The polarization directions of each simulated Mueller matrix and extinction matrix are fixed to their original incidence direction. This means the original polarization directions of the Mueller matrix and the extinction matrices change under rotation as indicated in Fig. 6. The rotation about the laboratory Z-axis by the Euler angle α does not change the polarization, because the vertical polarization direction stays always in the plane spanned by incidence direction unit vector $\hat{e}_{ki}$ and the laboratory z-axis and the horizontal polarization direction stays parallel to the x-y-plane. But the combined rotations by the Euler angles β and γ do change. After the combined rotation the original vertical polarization unit vector $\hat{e}_v$ is rotated out of the plane spanned by incidence direction unit vector $\hat{e}_{ki}$ and the laboratory z-axis by angle φ and original horizontal polarization unit vector $\hat{e}_h$ is rotated out of the x-y-plane by angle φ. After the rotation using $R_{\alpha\beta\gamma}$ the polarization of the Mueller matrix M and the extinction matrix K need to be transformed to the laboratory polarization using the stokes rotation matrix L (Mishchenko et al., 2002)

$$L(\varphi) = \begin{pmatrix} 1 & 0 & 0 & 0 \\ 0 & \cos 2\varphi & -\sin 2\varphi & 0 \\ 0 & \sin 2\varphi & \cos 2\varphi & 0 \\ 0 & 0 & 0 & 1 \end{pmatrix}. \tag{19}$$
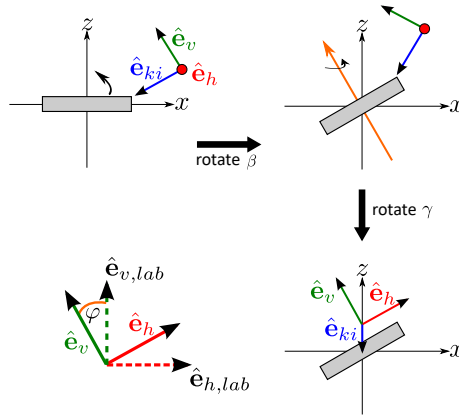
Figure 6. Change of the polarization directions under rotation. (top left) the incidence direction unit vector $\hat{e}_{ki}$ together with the vertical polarization unit vector $\hat{e}_v$ and the horizontal polarization unit vector $\hat{e}_h$, which are fixed to the particle, before the rotation is performed. (top right) the unit vectors after the rotation by angle β and (bottom right) after the rotation by angle γ. As indicated (bottom left) the polarization vectors after the rotation by angles β and γ are twisted by angle φ compared to the laboratory unit vectors.

The Mueller matrix M_{rot} and the extinction matrix K_{rot} of the rotated particle are given by

$$M_{rot} = R^*_{\alpha\beta\gamma}(M) = L(\varphi) M \left(R_{\alpha\beta\gamma}(\theta_{inc},\phi_{inc}), R_{\alpha\beta\gamma}(\theta'_s,\phi'_s) \right) L(-\varphi) \tag{20}$$

235   and

$$K_{rot} = R^*_{\alpha\beta\gamma}(K) = L(\varphi) K \left(R_{\alpha\beta\gamma}(\theta_{inc},\phi_{inc}) \right) L(-\varphi) . \tag{21}$$

The rotation angle φ is

$$\varphi = \text{atan2}\left(\hat{e}_v \cdot \hat{e}_{h,lab}, \hat{e}_v \cdot \hat{e}_{v,lab} \right) \tag{22}$$

with the rotated vertical polarization direction $\hat{e}_v$, the horizontal polarization direction in the laboratory system

240   $$\hat{e}_{h,lab} = \hat{e}_{v,lab} \times \hat{e}_{ki} , \tag{23}$$

the vertical polarization direction in the laboratory system

$$\hat{e}_{v,lab} = (\hat{e}_z \times \hat{e}_{ki}) \times \hat{e}_{ki} , \tag{24}$$

and z-direction $\hat{e}_z$.
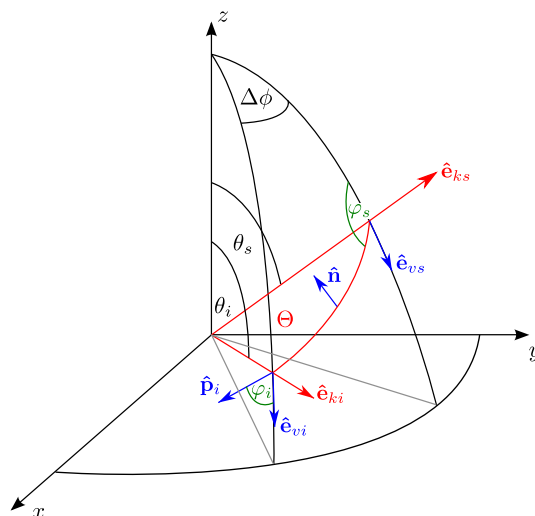
Figure 7. Scattering geometry in the laboratory system

4.2 Transformation of the averaged Mueller matrix to the averaged scattering matrix

245 Between the scattering matrix averaged Z and the averaged Mueller matrix M following relationship holds

$$Z(\theta_{inc}, \theta_s, \phi_s, \beta) = \frac{1}{k^2} L(-\varphi_s) M(\theta_{inc}, R(\theta_s', \phi_s'), \beta) L(\varphi_i) \tag{25}$$

with k the angular wave number, L the stokes rotation matrix (Eq. 19), φ_i, φ_s the polarization rotation angles, and $R(\theta_s', \phi_s')$ the rotation operator that transforms the incidence direction related coordinate system to the laboratory system.

As defined in Sect. 2.2, the incidence azimuth direction is zero. In that case the incidence direction vector is always within

250 the X-Z-plane. The rotation operator $R(\theta_s', \phi_s')$ then is

$$\begin{pmatrix} \theta_s \\ \phi_s \end{pmatrix} = R\begin{pmatrix} \theta_s' \\ \phi_s' \end{pmatrix} = \begin{pmatrix} \arccos\left(-\sin\theta_{inc}\sin\theta_s'\cos\phi_s' + \cos\theta_{inc}\cos\theta_s'\right) \\ \mathrm{atan2}\left(\sin\theta_s'\sin\phi_s', \cos\theta_{inc}\sin\theta_s'\cos\phi_s' + \sin\theta_{inc}\cos\theta_s'\right) \end{pmatrix}. \tag{26}$$

The stokes rotation matrices $L(-\varphi_s)$, $L(\varphi_i)$ transform the polarization basis from relative to the scattering direction to relative to incidence direction. Fig. 7 shows the geometry for polarization basis transformation. The stokes rotation matrix $L(-\varphi_s)$ describes the rotation by angle φ_s, which is the angle between the plane, that is spanned by the unit vector of the

255 scattering direction $\hat{e}_{ks}$ and the laboratory Z-axis, and the scattering plane, which is the plane that is spanned by the unit vector of the incidence direction $\hat{e}_{ki}$ and the unit vector of the scattering direction $\hat{e}_{ks}$. The stokes rotation matrix $L(\varphi_i)$ describes the rotation by angle φ_i, which is the angle between the plane that is spanned by the unit vector of the incidence direction and the

laboratory Z-axis, and the scattering plane. The unit vector $\hat{e}_{kj}$ describing the incidence or scattering direction is

$$\hat{e}_{kj} = \begin{pmatrix} \sin\theta_j \cos\phi_j \\ \sin\theta_j \sin\phi_j \\ \cos\theta_j \end{pmatrix} \tag{27}$$

260 and the unit vector of the vertical polarization $\hat{e}_{vj}$ for the incidence direction or the scattering direction is

$$\hat{e}_{vj} = \begin{pmatrix} \cos\theta_j \cos\phi_j \\ \cos\theta_j \sin\phi_j \\ -\sin\theta_j \end{pmatrix} \tag{28}$$

with $j = i, s$ for the incidence direction and the scattering direction, respectively. The rotation angle is

$$\varphi_j = \begin{cases} -\arccos(\hat{e}_{vj} \cdot \hat{p}_j) & , \hat{e}_{vj} \cdot \hat{n}_j \geq 0 \\ \arccos(\hat{e}_{vj} \cdot \hat{p}_j) & , \hat{e}_{vj} \cdot \hat{n}_j < 0 \end{cases} . \tag{29}$$

with the unit vector

265 $\hat{p}_j = \hat{n} \times \hat{e}_{kj}$ \hfill (30)

that is parallel to scattering plane and orthogonal to $\hat{e}_{kj}$. The normal vector

$$\hat{n} = \frac{\hat{e}_{ks} \times \hat{e}_{ki}}{\sin\Theta} \tag{31}$$

is orthogonal to the scattering plane. The scattering angle Θ, which is the angle between the incidence direction and the scattering direction is

270 $\sin\Theta = |\hat{e}_{ks} \times \hat{e}_{ki}|$ \hfill (32)

In the actual implementation each matrix element $M_{ij,aro}(\theta_{inc}, \theta'_s, \phi'_s)$ of the averaged Mueller matrix is represented as a spherical harmonics series over the scattering directions θ'_s, ϕ'_s. For the calculation of the averaged scattering matrix Z_{aro}, the Mueller matrix elements $M_{ij,aro}(\theta_{inc}, \theta'_s, \phi'_s)$ in angular grid representation are used. The resulting scattering matrix elements $Z_{ij,aro}$ in angular grid representation are expanded afterwards as spherical harmonics series over the scattering directions

275 θ_s, ϕ_{s_s}.

5   Results of the scattering simulations

In this section we give an overview of the scattering simulations and show some example results. 51 sizes of plate type 1 (hexagonal plate) and 18 sizes of large plate aggregates for 35 frequencies and 3 temperatures were simulated. The simulations

were conducted on DKRZ's (Deutsches Klimarechenzentrum) supercomputer Mistral. This took about $1.6 \cdot 10^6$ core hours
280 on Intel Xeon E5-2695V4 processors with a clock rate of 2.1Ghz. The amount of data of the scattering calculations is huge.
Whereas the scattering matrix $Z_{\text{tro}}(\Theta)$ for total random orientation depends on one angle, the scattering matrix $Z_{\text{aro}}(\theta_{inc}, \theta_s, \phi_s)$
for azimuthal random orientation depends on three angles. Furthermore, the tilt angle β adds an additional dimension. This leads
to an up to three orders of magnitude larger amount of data. To reduce the computation time and the amount of data, ADDA
was used with an accuracy of ϵ =1%. The Mueller and the scattering matrices for a given incidence angle were represented in a
285 truncated spherical harmonics series. with an accuracy of 0.5%. Even then, the total size of the data from the DDA simulations
is about 1.5 TB. Due to the orientation averaging the amount of data reduces to about 0.18 TB.

The orientation averaging is done for a finite set of incidence and tilt angles. The incidence angles θ_{inc} span a range from 0°
to 180° with a 5° spacing and the tilt angles β span a range from 0° to 90° for plate type 1 and from 0° to 180° for large plate
aggregates with a 10° spacing. The tilt angle range for plate type 1 is confined to 90°, because of its mirror symmetry to the
290 x-y plane. In this case it holds for the scattering matrix Z_{aro} and the extinction matrix K_{aro} that

$$Z_{\text{aro}}(\theta_{inc}, \theta_s, \phi_s, \beta) = Z_{\text{aro}}(\theta_{inc}, \theta_s, \phi_s, \pi - \beta)$$
$$K_{\text{aro}}(\theta_{inc}, \beta) = K_{\text{aro}}(\theta_{inc}, \pi - \beta)$$

(33)

The scattering database with the orientation averaged data is publicly available from Zenodo (https://doi.org/10.5281/zenodo.
3463003). The scattering database is organized so that the Python 3 interface of the database of Eriksson et al. (2018) can be
used to extract and interact with the data. The scattering database additionally includes for each incidence and tilt angle the
295 absorption vector a. The i-th component of the absorption vector is

$$a_i(\theta_{inc}, \beta) = K_{aro,i1}(\theta_{inc}, \beta) - \int\limits_0^{2\pi} \int\limits_0^{\pi} Z_{aro,i1}(\theta_{inc}, \theta_s, \phi_s, \beta) \, d\phi_s \, d\theta_s$$

(34)

with $K_{aro,i1}$ and $Z_{aro,i1}$ the i-th component of the first column of the extinction matrix K_{aro} and scattering matrix Z_{aro}
(Mishchenko et al., 2000).

In the following analysis we will not address the absorption vector, because it is derived directly from the extinction and
300 scattering matrix and is just added to the database for convenience.

5.1 Extinction matrix and asymmetry parameter

The orientation averaging (Eq. 16) reduces Eq. 10 to

$$K_{aro} = \frac{2\pi}{k} \begin{pmatrix} \text{Im}(S_{11}+S_{22}) & \text{Im}(S_{11}-S_{22}) & 0 & 0 \\ \text{Im}(S_{11}-S_{22}) & \text{Im}(S_{11}+S_{22}) & 0 & 0 \\ 0 & 0 & \text{Im}(S_{11}+S_{22}) & \text{Re}(S_{22}-S_{11}) \\ 0 & 0 & -\text{Re}(S_{22}-S_{11}) & \text{Im}(S_{11}+S_{22}) \end{pmatrix}$$

(35)

with S_{ii} the scattering amplitude matrix elements (Eq. 11) and k the angular wave number. Whereas the extinction matrix has
305 seven independent entries in general, the extinction matrix for azimuthal random orientation has only three independent entries

that depend on the incidence angle θ_{inc} and the tilt angle β. For total random orientation the extinction matrix has only one independent entry that is constant. Fig. 8 and Fig. 9 show the 3 independent entries of the extinction matrix (K_{11}, K_{21}, and K_{43}) of plate type 1 and large plate aggregate at 671 GHz for several tilt angles β and size parameters x

$$x = ka_{eq} = \frac{2\pi a_{eq}}{\lambda} = \frac{\pi D_{eq}}{\lambda} \tag{36}$$

310   with a_{eq} the volume equivalent frozen radius, D_{eq} the volume equivalent frozen diameter and λ the wavelength. For the large plate aggregate habit only size parameters $x > 3$ are shown, because for smaller sizes it is practically the same as plate type 1. The extinction matrix elements in Fig. 8 and Fig. 9 are normalized by the extinction cross section K_{tro} for total random orientation of the specific shape. Using Eq. 5 the extinction cross section for total random orientation K_{tro} is

$$K_{tro} = \int_0^\pi p_\beta(\beta) K_{aro,11}(\theta_{inc},\beta) \sin\beta\mathrm{d}\beta. \tag{37}$$

315   For the large plate aggregate, we skip the tilt angles $\beta > 90°$ in Fig. 9, because for $\beta > 90°$ the results are the same as for $\beta < 90°$ but mirrored around $\theta_{inc} = 90°$. Due to the mirror symmetry to the x-y plane of the hexagonal plates, the curves shown in Fig. 8 are symmetric relative to $\theta_{inc} = 90°$.

For the plate type 1 habit the effect of orientation and incidence angle results in differences of up to 50% of the $K_{aro,11}$ element compared to total random random orientation, whereas for the large plate aggregate habit the biggest differences

320   are at maximum about 15%. The biggest differences occur for tilt angles of 0° and 90° when looking from the top/bottom ($\theta_{inc} = 0°, 180°$) and from the side ($\theta_{inc} = 90°$). Depending on the size parameter, shape and magnitude of the curve change. For example, the maximum for the plate type 1 habit occurs at tilt angle $\beta = 0°$ and incidence angles of 0° and 180° for $x \lesssim 1$ and $x \approx 10$, whereas it occurs at an incidence angle of 90° for $x \approx 3$ and $x \approx 5$. The large plate aggregate habit shows a similar behavior albeit with much lower magnitude.

325   The $K_{aro,21}$ matrix element describes the extinction of the polarization difference between vertical and horizontal polarization and the $K_{aro,43}$ matrix element the extinction of polarization difference between the +45° and −45° polarization. For total random orientation, these matrix elements are zero, which is indicated by the gray line in Fig. 8 and Fig. 9. For the plate type 1 habit the $K_{aro,21}$ and the $K_{aro,43}$ matrix element show a strong dependency on the tilt angle and the incidence angle, which reduces with increasing size parameter. Except when looking from the top/bottom ($\theta_{inc} = 0°, 180°$) both elements are

330   non-zero. For the large plate aggregate habit the $K_{aro,21}$ and the $K_{aro,43}$ matrix element are practically zero showing only small deviations from zero for $x \gtrsim 3$.

The results for the plate type 1 with $x \approx 1.4$ and tilt angle $\beta = 0°$ agree qualitatively with the results of Adams and Bettenhausen (2012) for azimuthally randomly oriented hexagonal plates with tilt angle $\beta = 0°$ and a similar size parameter but at a different frequency. Adams and Bettenhausen (2012) simulated for microwave frequencies among others the scattering of

335   azimuthally randomly oriented hexagonal plates with tilt angle $\beta = 0°$.

The asymmetry parameter describes the distribution between forward scattering and backscattering and gives an overview of the scattering behavior. For example, $g = 0$ means forward scattering and backscattering are of equal strength, whereas

$g = 1$ and $g = -1$ mean only forward scattering and only backscattering, respectively. The asymmetry parameter for azimuthal random orientation is

$$340 \quad g_{aro}(\theta_{inc}, \beta) = \frac{1}{2} \int\limits_{0}^{2\pi} \int\limits_{0}^{\pi} \cos(\theta_s - \theta_{inc}) Z_{aro,11}(\theta_{inc}, \theta_s, 0, \phi_s, \beta) \, d\phi_s d\theta_s \tag{38}$$

with $Z_{aro,11}$ being the $(1,1)$-element of the scattering matrix Z_{aro}. The asymmetry parameter is shown in Fig. 8 and Fig. 9. The asymmetry parameters for the different tilt angles are centered around the asymmetry parameter g_{tro} for total random orientation, which is shown as gray line. The asymmetry parameter g_{tro} for total random orientation is calculated by integrating $g_{aro}(\theta_{inc}, \beta)$ over the tilt angle β similar to Eq. 37. For $x \ll 1$, the total random orientation asymmetry parameter g_{tro} is zero

345   indicating symmetric forward and backward scattering as expected for Rayleigh scattering. With increasing size parameter forward scattering increases. The azimuthal random orientation asymmetry parameter g_{aro} for the large plate aggregate habit deviates slightly from the total random orientation asymmetry parameter g_{tro} with changing tilt angle β, whereas for the plate type 1 habit it deviates strongly from the total random orientation asymmetry parameter g_{tro} especially for $1 < x < 6$. For example, at tilt angle $\beta = 0°$ and incidence angles of $0°$ and $180°$ for $x = 1.4$ the scattering in forward and backward direction

350   is almost symmetric but at tilt angle $\beta = 90°$ the scattering in forward direction is much stronger than in backward direction.

5.2 Scattering matrix

The scattering matrix of a particle describes the angular distribution of the scattered radiation in relation to the incidence direction of the incoming radiation. For unpolarized incoming radiation, the Z_{j1}-element with $j = \{1, ..., 4\}$ show the angular distribution of the scattered radiation field. For example, the Z_{11}-element shows the angular distribution of the scattered inten-

355   sity (I component of the Stokes vector), whereas the Z_{21}-element shows how and where the scattered radiation is horizontally and vertically polarized (Q component of the Stokes vector) due to the scattering. Negative Z_{21} values mean that the horizontal polarization dominates and vice versa. For polarized radiation, the j-th component of the scattered radiation field depends additionally on the coupling with the other components of the incoming Stokes vector, which is described by the Z_{ji}-element with $i = \{2, 3, 4\}$.

360   After the orientation averaging, the resulting scattering properties possess a rotational symmetry relative to the laboratory z-axis. The scattering matrix Z_{aro} (Eqn. 15, 25) depends for tilt angle β on the polar incidence angle θ_{inc}, the polar scattering angle θ_s and the scattering azimuth angle ϕ_s. In contrast, the scattering matrix of totally randomly oriented particles depends only on the scattering angle Θ. The different tilt angles β result in different effective shapes and therefore different scattering matrices. The impact of the tilt angle β depends also on the incidence direction and is different for the different scattering

365   matrix elements.

As an example, Fig. 10 shows at $671\,\text{GHz}$ and for several incidence angles θ_{inc} and tilt angles β the upper left block of the normalized scattering matrix $\hat{Z}_{aro}(\theta_{inc}, \theta_s, \phi_s)$ of plate type 1 for size parameter $x \approx 3$. The normalized scattering matrix
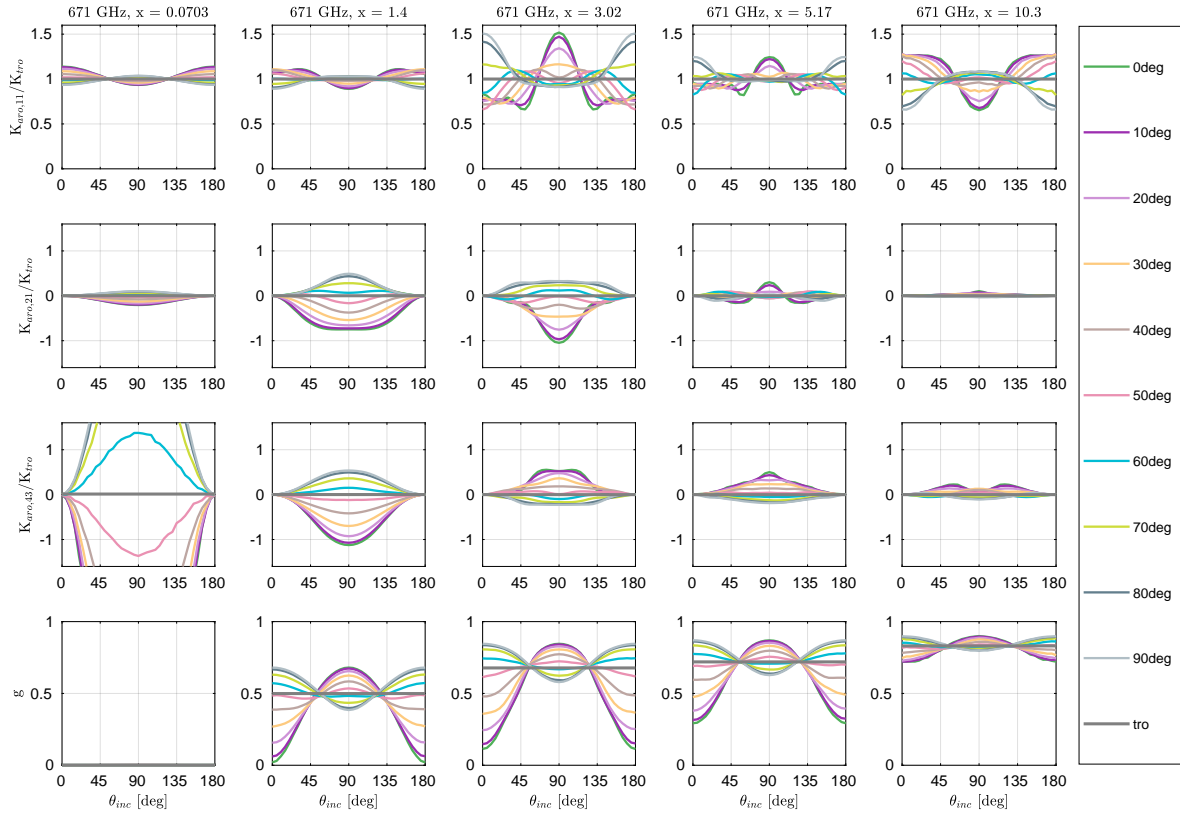
Figure 8. Extinction matrix elements $K_{aro,ij}$ normalized by the extinction cross section for total random orientation and the asymmetry parameter ⊠ of plate type 1 (hexagonal plate) for different size parameter x at 671 GHz as function of incidence angle θ_{inc} for several tilt angles β. The gray lines denote total random orientation. The shapes of the scatterers are shown in Fig. 3.

$\hat{Z}_{\text{aro}}(\theta_{inc}, \theta_s, \phi_s)$ is

$$\hat{Z}_{\text{aro}}(\theta_{inc}, \theta_s, \phi_s) = 4\pi \frac{Z_{aro}}{\int_0^{2\pi} \int_0^{\pi} Z_{\text{aro}}(\theta_{inc}, \theta_s, \phi_s) \, d\phi_s \, d\theta_s} . \tag{39}$$

370 We show only the upper left block, because these are the most relevant entries of the scattering matrix considering the present spaceborne microwave and submillimeter wave sensors, but all 16 elements are calculated. At incidence direction $\theta_{inc} = 0°$, the $\hat{Z}_{11}$- and $\hat{Z}_{22}$-element differ strongly between the different tilt angles β. Especially in the backscattering direction they strongly decrease with increasing tilt angle β. The $\hat{Z}_{21}$- and $\hat{Z}_{12}$-element show only slight differences between the different tilt angles. Whereas the $\hat{Z}_{11}$-element decreases at backscattering direction with increasing tilt angle, it is fairly constant at the forward

375 direction resulting in total in an increased forward direction, which is also shown by the asymmetry parameter ⊠$_{aro}$ in Fig. 8.
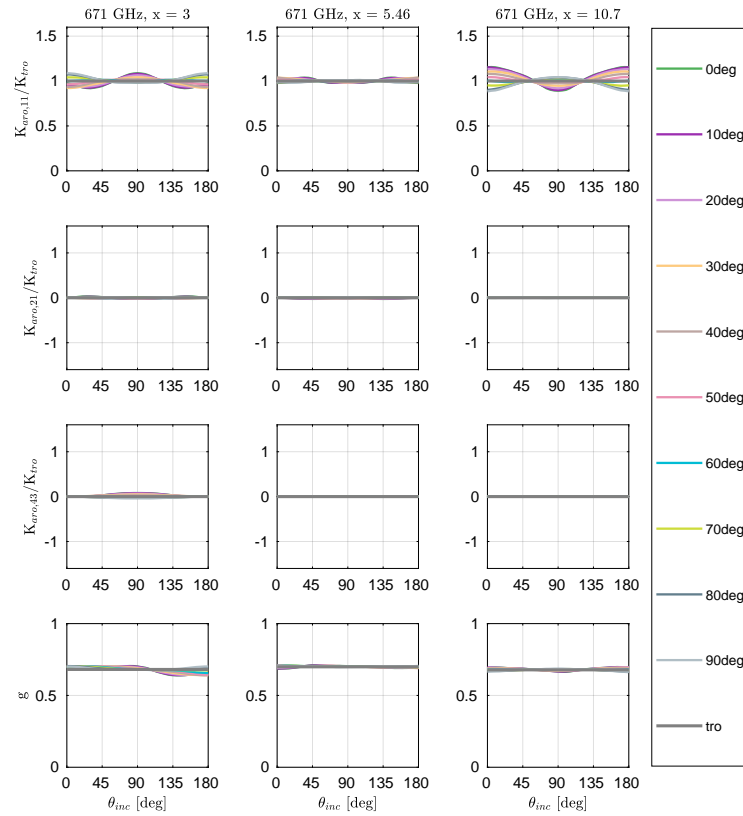
Figure 9. Extinction matrix elements $K_{aro,ij}$ normalized by the extinction cross section for total random orientation and the asymmetry parameter ⬚ of large plate aggregate (hexagonal plate aggregate) for different size parameter x at 671 GHz as function of incidence angle θ_{inc} for several tilt angles β. The gray lines denote total random orientation. The shapes of the scatterers are shown in Fig. 3.

Within the Rayleigh regime ($x \ll 1$, not shown) the influence of the tilt angle β on the normalized scattering matrix $\hat{Z}_{aro}$ is negligible at incidence direction $\theta_{inc} = 0°$.

For non nadir/zenith incidence directions the $\hat{Z}_{21}$- and $\hat{Z}_{12}$- element as well the other scattering matrix elements differ strongly for different tilt angle β. For example, the $\hat{Z}_{21}$- and $\hat{Z}_{12}$- elements have a negative peak at $\theta_s = 180° - \theta_{inc}$ and $\phi_s = 0°$
380   for tilt angle $\beta = 0°$, which means that incoming unpolarized radiation scattered at this direction is horizontally polarized. There is no peak at this scattering direction for tilt angle $\beta = 30°$ or $\beta = 90°$. For tilt angle $\beta = 30°$ there is a negative peak at $\theta_s = \theta_{inc}$ and for tilt angle $\beta = 90°$ there is a positive peak at $\theta_s = \theta_{inc}$. The negative peaks of the $\hat{Z}_{21}$- and $\hat{Z}_{12}$- element at $\theta_s = 180° - \theta_{inc}$ and $\phi_s = 0°$ for $\beta = 0°$ are accompanied by peaks of the $\hat{Z}_{11}$- and $\hat{Z}_{22}$-element. For tilt angle $\beta = 30°$ or $\beta = 90°$ the $\hat{Z}_{11}$- and $\hat{Z}_{22}$-elements do not have peaks at that direction but only in the forward direction $\theta_s = \theta_{inc}$. The peak
385   at $\theta_s = 180° - \theta_{inc}$ and $\phi_s = 0°$ for tilt angle $\beta = 0°$ coincides with the specular reflection direction of a plane. The results of

Adams and Bettenhausen (2012) for the $\hat{Z}_{11}$- and the $\hat{Z}_{21}$- element for size parameter $x \approx 4$ fit qualitatively with the $\hat{Z}_{11}$- and the $\hat{Z}_{21}$-element for tilt angle $\beta = 0°$ in Fig. 10. Interestingly, the large plate aggregate in Fig. 11 with similar size parameter x as the plate type 1 habit in Fig. 10 does not show these peaks. There is also no strong backscattering for nadir incidence direction. Fig. 11 shows at 671 GHz and for several incidence angles θ_{inc} and tilt angles β the upper left block of the normalized scattering

390   matrix $\hat{Z}_{\mathrm{aro}}(\theta_{inc}, \theta_s, \phi_s)$ of large plate aggregate for size parameter $x \approx 3$. Compared to the plate type 1 habit in Fig. 10 the $\hat{Z}_{21}$- and $\hat{Z}_{12}$-elements are practically zero. This means unpolarized incoming radiation scattered by the large plate aggregate does not show much polarization. On the other hand, at 167 GHz the $\hat{Z}_{21}$- and $\hat{Z}_{12}$-elements are non zero and significantly differ between the different tilt angles β. Fig. 12 shows at 167 GHz and for several incidence angles θ_{inc} and tilt angles β the upper left block of the normalized scattering matrix $\hat{Z}_{\mathrm{aro}}(\theta_{inc}, \theta_s, \phi_s)$ of the same large plate aggregate as in Fig. 11. At 167 GHz the

395   size parameter for this particle is $x \approx 0.75$. Compared to Fig. 11 the scattering is less focused toward the forward scattering direction.

The data from the simulated scattering matrix can be used for simulations of passive and active observations. However, for simulations of horizontally scanning radars the scattering matrix in the backscattering direction has to be handled with care. In the spherical harmonics representation of the Mueller matrix, the polarization at the poles, which are in the forward and

400   backward direction, is not well represented. This can result in errors for the polarization. Most of this is averaged out due to the orientation averaging and the transformation to the scattering matrix, but there can be some residual effects for the polarization at the backscattering direction. This will be revised for the next iteration of the database.

6   Radiative transfer simulations

In this section, we show radiative transfer simulations at 166 GHz using azimuthally randomly oriented scatterers in order to

405   give an example of the capabilities of the simulated scattering data. For the radiative transfer simulations, 200 atmospheric profiles over the tropical pacific were taken from one of the EarthCARE scenes. These scenes were prepared for the EarthCARE mission with Environment Canada's high-resolution numerical weather prediction model known as the Global Environmental Multiscale Model (GEM, Côté et al., 1998). The GEM scenes have a resolution of 250 m and include two liquid hydrometeor species (rain, liquid clouds) and four frozen hydrometeor species (cloud ice, snow, graupel, and hail). The profiles were

410   randomly selected except for that they should cover the whole possible brightness temperature space as uniformly as possible.

The simulations were done using the Atmospheric Radiative Transfer Simulator (ARTS, Buehler et al., 2018; Eriksson et al., 2011) version 2.3.1118. The discrete ordinate iterative solver (DOIT, Emde, 2004) was used as scattering solver within ARTS. The simulations of Rayleigh–Jeans brightness temperatures were done using independent pixel approximation (IPA) with a local incidence angle of 49° for a satellite orbit height of 407 km at 164.1 GHz and 166.9 GHz, which were averaged

415   to mimic the GMI's 166 GHz channel. Within ARTS, gas absorption was taken into account by using the HITRAN data base (Rothman et al., 2013) and the MT_CKD model for the continuum absorption of water vapor and molecular nitrogen in version 2.52 (Mlawer et al., 2012). The gas absorption of molecular oxygen was processed by using the full absorption model of Rosenkranz (1998) modified by the values from Tretyakov et al. (2005). The ocean surface emissivity was calculated with
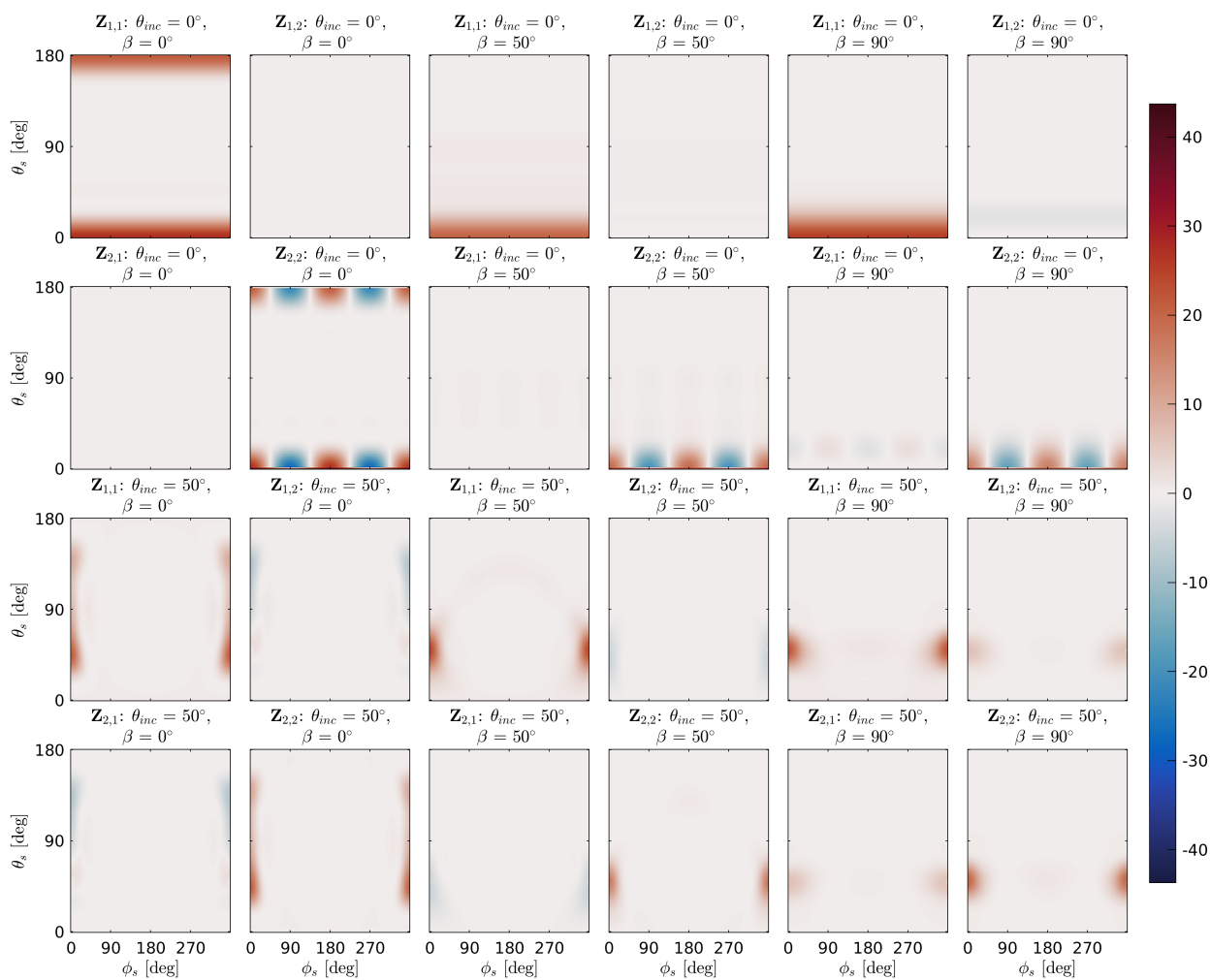
Figure 10. The upper left block of the normalized scattering matrix $\hat{Z}$ of plate type 1 with a volume equivalent diameter of $429\,\mu m$ (Fig. 3) and a size parameter $x \approx 3$ at $671\,GHz$ as function of the polar scattering angle θ_s and the azimuth scattering angle ϕ_s for a set of tilt angles β and incidence angles θ_{inc}.
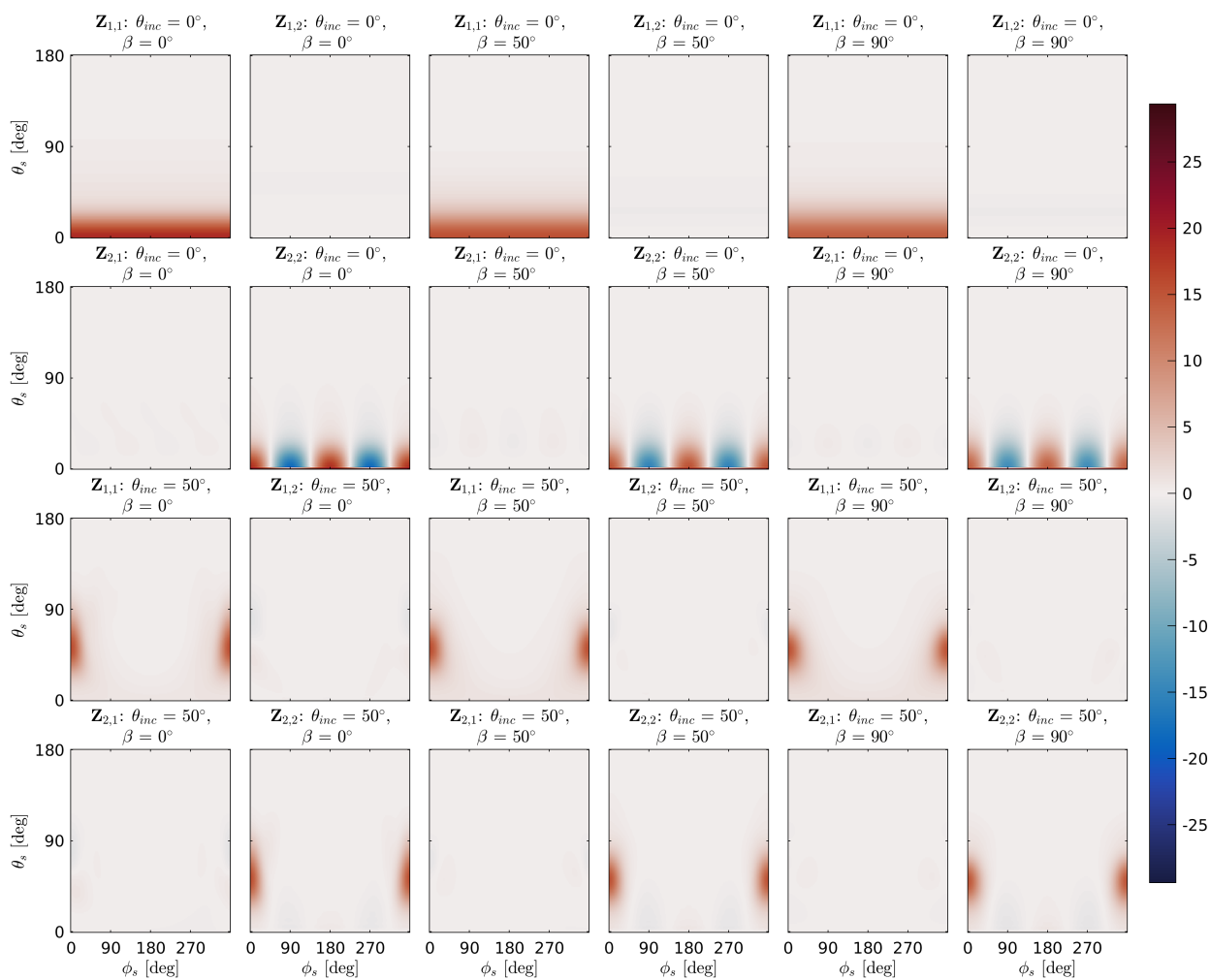
Figure 11. The upper left block of the normalized scattering matrix $\hat{\mathbf{Z}}$ of large plate aggregate with a volume equivalent diameter of $427\,\mu\mathrm{m}$ (Fig. 3) and a size parameter $x \approx 3$ at $671\,\mathrm{GHz}$ as function of the polar scattering angle θ_s and the azimuth scattering angle ϕ_s for a set of tilt angles β and incidence angles θ_{inc}.
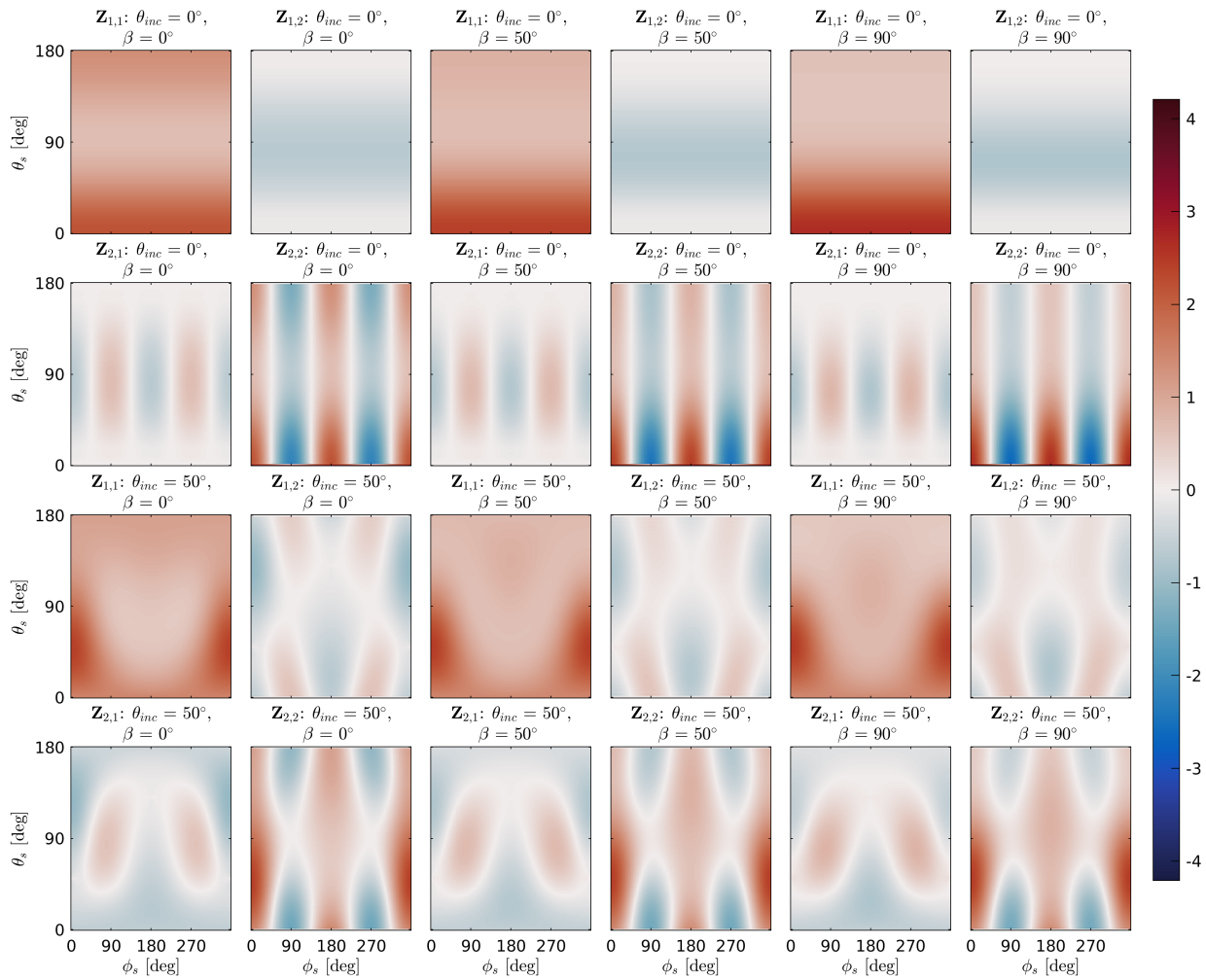
Figure 12. The upper left block of the normalized scattering matrix $\hat{Z}$ of large plate aggregate with a volume equivalent diameter of $427\,\mu m$ (Fig. 3) and a size parameter $x \approx 0.75$ at $167\,GHz$ as function of the polar scattering angle θ_s and the azimuth scattering angle ϕ_s for a set of tilt angles β and incidence angles θ_{inc}.

Table 3. Size distribution parameters and the scatterer shape of the radiative transfer simulations. The size distribution parameters were taken from the source code of the Milbrandt-Yau two-moment bulk microphysics (Milbrandt and Yau, 2005a, b) of the GEM model. Except for cloud ice and snow the scattering properties were taken from Eriksson et al. (2018).

	MGD parameter		scatterer habits		
	ν	μ	Fig. 13	Fig. 14	Fig. 16
cloud water	1	1	Liquid Sphere, ID 25	Liquid Sphere, ID 25	Liquid Sphere, ID 25
rain	0	1	Liquid Sphere, ID 25	Liquid Sphere, ID 25	Liquid Sphere, ID 25
cloud ice	0	1	Plate Type 1 (ARO)	Plate Type 1 (ARO)	Plate Type 1 (ARO)
snow	0	1	Large plate aggr. (ARO)	Large plate aggr. (ARO)	Plate Type 1 (ARO)
graupel	0	1	GEM Graupel, ID 33	-	GEM Graupel, ID 33
hail	0	1	GEM Hail, ID 34	GEM Hail, ID 34	GEM Hail, ID 34

the Tool to Estimate Sea-Surface Emissivity from Microwaves to sub-Millimeter waves (TESSEM2, Prigent et al. (2017))
420 implementation within ARTS using the surface speed and temperature from the GEM profiles.

The Milbrandt-Yau two-moment microphysics (Milbrandt and Yau, 2005a, b) implementation within ARTS with the same hydrometeor types and size distributions as for the GEM runs was used. The Milbrandt-Yau two-moment microphysics assumes a modified gamma distribution with characteristic parameters for each individual hydrometeor;

$$N(x) = N_0 x^\nu \exp(-\lambda x^\mu) \qquad (40)$$

425 with the parameters N_0 and λ, which are functions of the number density and the hydrometeor content and parameters μ and ν. The parameters μ and ν are fixed for each hydrometeor type and are summarized in Table 3. The Milbrandt-Yau two-moment bulk microphysics use the particle maximum diameter as independent variable x for the size distribution.

The scattering properties for the hydrometeors were taken from Eriksson et al. (2018) except for cloud ice and snow. The database of Eriksson et al. (2018) contains among others the single scattering properties of hydrometeors, which are modeled
430 to be consistent with the m-D parameters of the Milbrandt-Yau two-moment bulk microphysics scheme. The particles inside the database of Eriksson et al. (2018) are assumed to be totally randomly oriented.

For cloud ice and snow the azimuthally randomly oriented plate type 1 and the azimuthally randomly oriented large plate aggregate are used. For the simulations the azimuthally randomly oriented particles are orientation-averaged over Gaussian distributed β angles with zero mean and increasing standard deviation. 6 different orientation states were prepared for the
435 simulations to mimic different stages of fluttering of the particle. Additionally, the azimuthally randomly oriented particles were averaged over uniformly distributed β angle to show the results for total random orientation. The used single scattering properties are summarized in Table 3.

6.1 Results and discussion

Fig. 13 shows the vertical polarization of the brightness temperature T_{bv} and the polarization difference $T_{bv} - T_{bh}$ as function

440 of the frozen water path (FWP) for the different orientations. The FWP is the sum of each vertically integrated mass content of the four frozen hydrometeors. The plate type 1 habit for ice clouds and the large plate aggregate habit for snow were used for the simulation, see Table 3 for the other hydrometeors. The vertical polarization of the brightness temperature T_{bv} decreases from $\approx 280\,\mathrm{K}$ at a FWP of $\approx 10^{-2}\,\mathrm{kg\,m^{-2}}$ with increasing frozen water path to $\approx 85\,\mathrm{K}$ at a FWP of $\approx 20\,\mathrm{kg\,m^{-2}}$. The polarization difference $T_{bv} - T_{bh}$ increases with increasing FWP till a maximum is reached at a FWP of $\approx 5\,\mathrm{kg\,m^{-2}}$ and then decreases with

445 increasing FWP. The maximum of the polarization difference depends on the orientation state. For total horizontal orientation the maximum polarization difference is $\approx 11\,\mathrm{K}$. With increased standard deviation (fluttering) the maximum polarization difference decreases down to $\approx 2.5\,\mathrm{K}$ for totally randomly oriented particles. The orientation depending polarization difference also indicates that particle orientation is not only an issue for dual polarized observations but also for single polarized observations. Ignoring orientation can cause a negative bias for vertically polarized observations and in a positive bias for horizontally

450 polarized observations.

Additionally, Fig. 13 shows the polarization difference $T_{bv} - T_{bh}$ as function of the vertical polarized brightness temperature T_{bv}. The polarization difference has a bell like distribution with a flat top and its maximum at $\approx 195\,\mathrm{K}$ for total horizontal orientation. With increased standard deviation the curve gets flatter. For small standard deviations ($\leq 10°$) the bell like distributions of the polarization difference are similar to the mean polarization differences that Gong and Wu (2017) estimated

455 from GMI measurements over tropical ocean and the mean polarization differences that Defer et al. (2014) estimated from MADRAS. The results of Gong and Wu (2017) and of Defer et al. (2014) are addionally shown in Fig. 13 as gray solid and dashed lines. Though MADRAS has a slightly higher incidence angle than GMI and measures at $157\,\mathrm{GHz}$ instead of $166\,\mathrm{GHz}$, the observations of GMI and MADRAS are similar.

Additional tests show that the polarization difference and the brightness temperature are mainly influenced by snow and

460 graupel. For these tests (not shown) one hydrometeor at a time was set to zero, while the others were unchanged, and the simulations for the 200 profiles and 7 orientation states were rerun. Cloud liquid and rain have impact on single profiles but do not change the overall behavior of the polarization difference. The influence of ice clouds is negligible, because most of the ice cloud particles are too small to cause significant scattering at $166\,\mathrm{GHz}$. Hail does not need to be considered, because within the 200 profiles its content is very little and therefore does not cause any significant scattering. Setting graupel or snow to zero

465 strongly alters the polarization difference and the brightness temperature.

For the simulations shown in Fig. 14 the mass content and number density of graupel was added to snow but without changing the total amount of frozen water mass content and the other hydrometeors. In this case snow is the only significant cause of scattering. Compared to Fig. 13 the minimum brightness temperature T_{bv} is higher by $\approx 40\,\mathrm{K}$, which means that the scattering of the large plate aggregate habit is weaker than the graupel habit. The reason for that is that the graupel habit due

470 to its higher density has a larger scattering coefficient than the large plate aggregate. More interesting is how the polarization differs. The polarization difference $T_{bv} - T_{bh}$ distribution has indications of a bell like distribution but compared to Fig. 13

it does not reach zero for the minimum brightness temperature T_{bv} and it is flatter. Furthermore, the polarization difference maximum is shifted by $\approx 30\,\mathrm{K}$ to lower brightness temperature and is slightly higher. Down to $T_{bv} \approx 170\,\mathrm{K}$ the polarization differences for small standard deviations ($\leq 10°$) are similar to the observed polarzation differences of Gong and Wu (2017)

475 and of Defer et al. (2014). For $T_{bv} \lesssim 170\,\mathrm{K}$ the polarization differences are larger than the observed ones. Around brightness temperature $T_{bv} = 125\,\mathrm{K}$, approximately the minimum brightness temperature, the polarization difference is roughly twice as for the similar brightness temperature in Fig. 13 and the observations of Gong and Wu (2017) and of Defer et al. (2014).

The bell like distribution of the polarization difference $T_{bv} - T_{bh}$ in Fig. 14 is caused by two opposing effects. On one hand increasing the amount of scatterers results in increased scattering and in increased polarization difference. On the other hand,

480 increasing the amount of scatterers results in increased multi-scattering and in decreased polarization difference. For small amount of scattering the polarization increase dominates and for large amount of scattering polarization decrease dominates.

In Fig. 14 snow is the only significant cause of scattering, whereas in Fig. 13 snow and graupel are the causes of scattering. The smaller polarization differences in Fig. 13 compared to Fig. 14 for brightness temperatures $T_{bv} < 220\,\mathrm{K}$ show that not only multi-scattering reduces the polarization but also the composition of the scatterers. As the amount of frozen particles increases

485 the composition changes. For small amount of frozen hydrometeors the amount of snow dominates whereas the amount of graupel dominates for large amount of frozen hydrometeors, see Fig. 15. Graupel is simulated by the GEM graupel habit of the database of Eriksson et al. (2018). Due to its total random orientation and its sphere like shape the GEM graupel habit causes only negligible polarization at 166 GHz. For small amount of frozen hydrometeors snow dominates the scattering and increasing the amount of frozen hydrometeors results in increased scattering and in increased polarization difference. With

490 increasing amount of frozen hydrometeors not only multi-scattering increases but also the scattering due to graupel. Both decreases the polarization difference. Due to this the polarization difference in Fig. 13 is smaller for $T_{bv} < 220\,\mathrm{K}$ and the maximum polarization difference is at higher brightness temperatures than in Fig. 14.

As an additional scenario, the large plate aggregate habit for snow was replaced by the plate type 1 habit and the simulations for the 200 profiles and 7 orientation states were rerun, which is shown in Fig. 16. The polarization difference $T_{bv} - T_{bh}$

495 distribution has similar shape as in Fig. 13 but it has a roughly three times higher magnitude and a much higher spread, whereas the brightness temperature T_{bv} differs only slightly. This shows that the polarization difference not only depends on the orientation but on the shape, too. For a standard deviation of $\approx 40°$ the bell like distribution of the polarization difference is comparable to the mean polarization differences of Gong and Wu (2017) and of Defer et al. (2014).

The comparison of the three different scenarios with the observations of Gong and Wu (2017) and of Defer et al. (2014)

500 shows that snow simulated as large plate aggregate with small standard deviations ($\leq 10°$) or as plate type 1 with standard deviations in the order of $O(40°)$ is compatible with the observations, if additionally graupel is included within the simulations. Without graupel, the observed decrease of the polarization differences for brightness temperature $T_{bv} < 170\,\mathrm{K}$ cannot be reached.
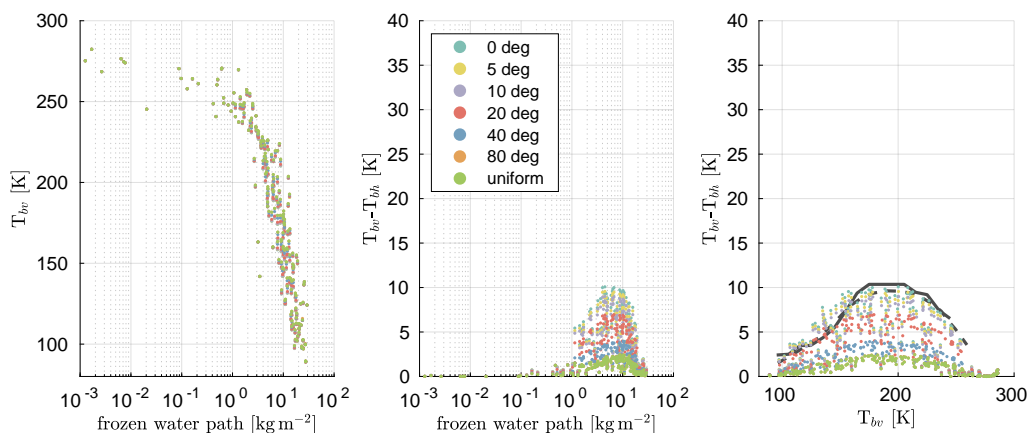
Figure 13. Simulated brightness temperature at 166 GHz for 200 randomly selected atmospheric profiles. For each of these atmospheric profiles the scattering properties of the azimuthally randomly oriented scatterers are orientation averaged over 7 different distributed β angles with zero mean and different standard deviation. The different colors denote the standard deviation of the β angle distribution and the distribution type. For the used scatterers, see Table 3. The gray line solid line denotes the mean polarization difference over tropical ocean from GMI observations at 166 GHz of Gong and Wu (2017) and the gray dashed line the mean polarization difference over tropical ocean from MADRAS observations at 157 GHz of Defer et al. (2014).
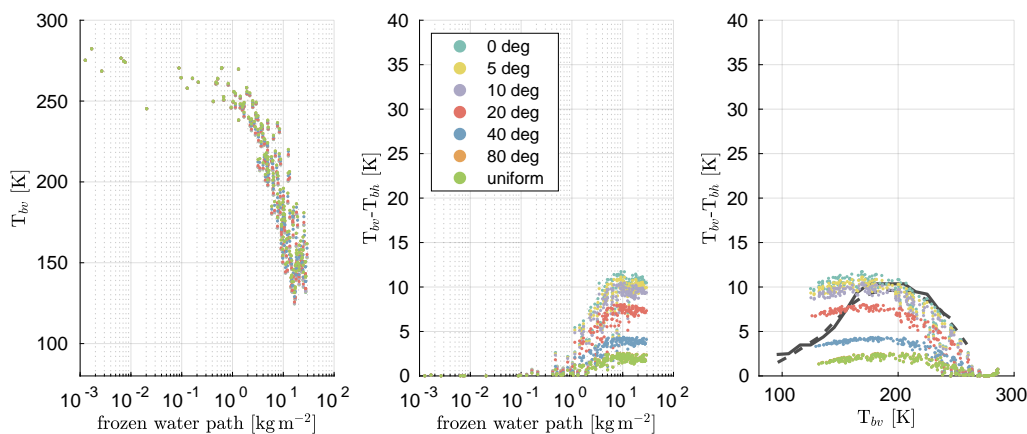
Figure 14. Same as Fig. 13 but the mass content and the number density of graupel added to snow.
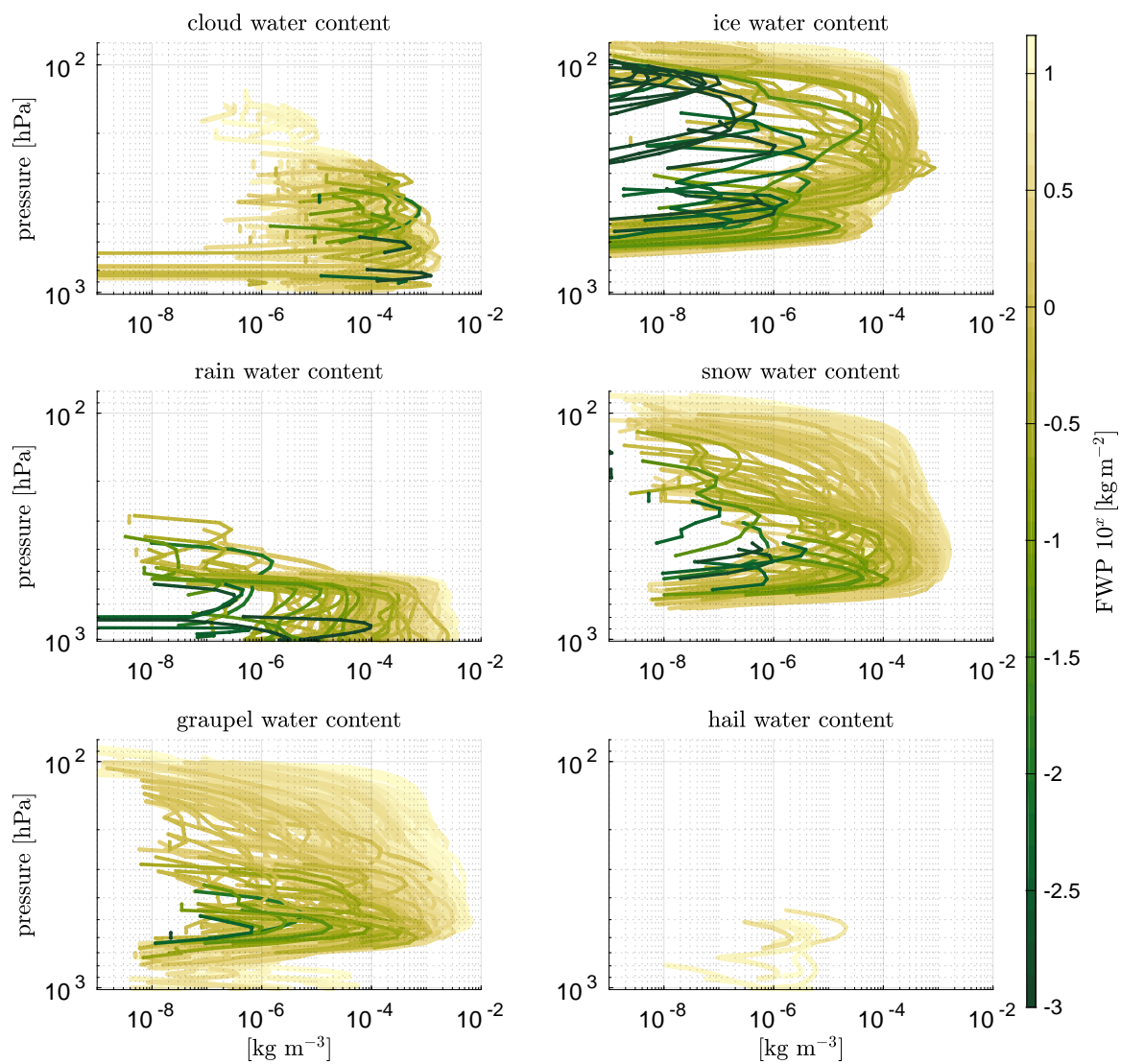
Figure 15. Hydrometeor content profiles used for the radiative transfer simulation in Fig. 13. The color indicates the frozen water path (FWP) of each atmospheric profile.
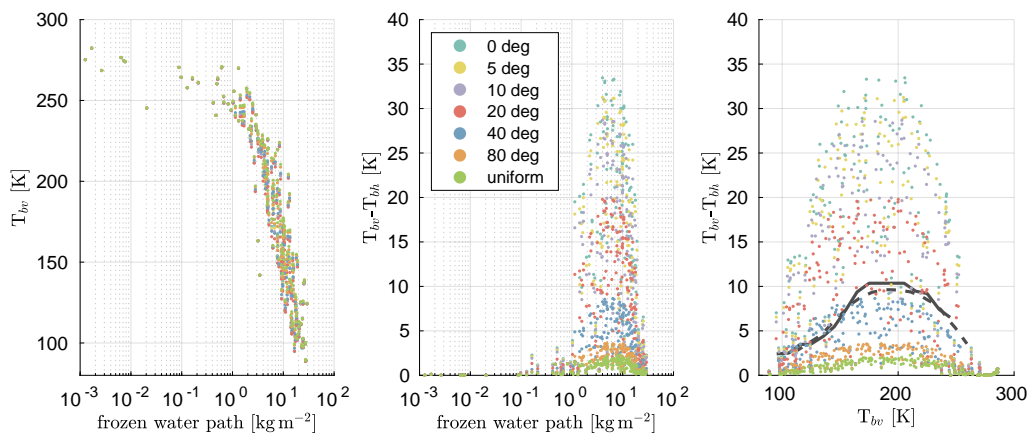
Figure 16. Same as Fig. 13 but with plate type 1 for snow instead of large plate aggregate.

7 Summary

505 We provide microwave and submillimeter wave scattering simulations of azimuthally randomly oriented ice crystals with a fixed but arbitrary tilt angle. For the simulations, DDA simulations made with ADDA were combined with a self developed orientation averaging approach. The scattering of 51 sizes of hexagonal plates (plate type 1) between $10\,\mu m$ and $2,596\,\mu m$ volume equivalent diameter and 18 sizes of hexagonal plate aggregates (large plate aggregate) between $197\,\mu m$ and $4,563\,\mu m$ for 35 frequencies between $1\,GHz$ and $864\,GHz$ and 3 temperatures ($190\,K$, $230\,K$, $270\,K$) were simulated. The scattering data

510 for azimuthal random orientation is much more complex than for total random orientation. Whereas for total random orientation the scattering matrix $Z_{tro}(\Theta)$ depends only on one angle and the extinction matrix K_{tro} has no angular dependency at all and has only one independent entry, for azimuthal random orientation the scattering matrix $Z_{aro}(\theta_{inc}, \theta_s, \phi_s)$ depends on three angles and the extinction matrix $K_{aro}(\theta_{inc})$ depends on the incidence angle and has three independent entries. Furthermore, the tilt angle β adds an additional dimension. For a finite set of incidences and tilt angles, in which the incidence angles θ_{inc} span a

515 range from $0°$ to $180°$ with a $5°$ spacing and the tilt angles β span a range from $0°$ to $90°$ for plate type 1 and from $0°$ to $180°$ for large plate aggregates with a $10°$ spacing, the scattering data has a size of $181\,GB$, which is roughly 20 times bigger than the whole database of Eriksson et al. (2018). The scattering database of the azimuthally randomly oriented particles is publicly available from Zenodo (https://doi.org/10.5281/zenodo.3463003). The scattering database is organized so that the Python 3 interface of the database of Eriksson et al. (2018) can be used to extract and interact with the data.

520 To give an example of the capabilities of the dataset, we conducted radiative transfer simulations of polarized GMI measurements of differently fluttering ice crystals at $166\,GHz$. The radiative transfer simulations were conducted using ARTS (Buehler et al., 2018; Eriksson et al., 2011) and assuming Milbrandt-Yau two-moment microphysics (Milbrandt and Yau, 2005a, b) with two liquid hydrometeor species (rain, liquid clouds) and four frozen hydrometeor species (cloud ice, snow, graupel, and hail). For slightly fluttering snow and ice particles, the simulations show polarization differences up to $11\,K$ using the azimuthally

525   randomly oriented large plate aggregate habit for snow, the plate type 1 habit for cloud ice and totally oriented particles for the
other four hydrometeors. The simulations cover the observed brightness temperatures and polarization differences from Gong
and Wu (2017) and Defer et al. (2014). Further analysis shows that not only multi-scattering affects the polarization but also
the hydrometeor composition. The polarization difference and the brightness temperature are mainly influenced by snow and
graupel. Exchanging the large plate aggregate habit with the plate type 1 habit for snow results in roughly three times bigger

530   polarization difference. For strongly fluttering snow and ice particles, the simulations using the plate type 1 habit for snow
and ice are similar to Gong and Wu (2017) and Defer et al. (2014). Particle orientation also affects single polarized observa-
tions. Ignoring orientation can cause a negative bias for vertically polarized observations and in a positive bias for horizontally
polarized observations.

Using the new scattering data for retrievals of polarized observations from GMI, MADRAS and especially the upcoming ICI

535   can give us new insights for the understanding of clouds. For example, to the authors' knowledge none of the latest atmospheric
weather and climate models handle orientation. Furthermore, polarization can give us additional informations on the shape of
the particle.

Data availability.   The scattering database of the azimuthally randomly oriented particles is publicly available from Zenodo (https://doi.org/
10.5281/zenodo.3463003). The data of the radiative transfer simulations of Sect. 6 is also publicly available from Zenodo (https://doi.org/10.

540   5281/zenodo.3475897).

Competing interests.   The authors declare that they have no conflict of interest.

Author contributions.   Manfred Brath has developed the orientation averaging approach, set up and conducted the scattering and the radiative
transfer simulations and written the article's text. Robin Ekelund prepared the scatterer shape data, designed the database structure and
contributed text. Patrick Eriksson has acted as project leader and initiated the database. Patrick Eriksson and Stefan A. Buehler participated

545   in planning of the database and have contributed text. Oliver Lemke helped to set up and to conduct the scattering simulations and prepared
the data for publication.

Acknowledgements.   A large part of this work was produced inside a study funded by EUMETSAT (Contract No. EUM/COS/LET/16/879389).
The study manager at EUMETSAT was Christophe Accadia, who provided appreciated feedback and inspiration. Robin Ekelund and Patrick
Eriksson were further supported financially by the Swedish National Space Agency (SNSA) under grant 150/14. The authors would like to

550   thank Howard Barker from Environment and Climate Change Canada for providing the GEM model simulations. Stefan A. Buehler was
supported by the Deutsche Forschungsgemeinschaft (DFG, German Research Foundation) under Germany's Excellence Strategy — EXC

2037 'Climate, Climatic Change, and Society' — Project Number: 390683824, contributing to the Center for Earth System Research and Sustainability (CEN) of Universität Hamburg. Finally, our thanks to the ARTS radiative transfer community for their help with using ARTS.

Appendix A: Initial particle alignment

Before any orientation averaging can be performed, the initial orientation of the particle has to be defined. The alignment algorithm is based mainly on aligning the principal moments of inertia axes along the Cartesian coordinate axes. Also, a number of special cases are treated in order to make the alignment consistent between particles and not dependent on small numerical differences. The result of the algorithm is that the particle fulfills the following criteria: the principal axis of the particle with the largest inertia is aligned along the z-axis, and its principal axis with the smallest inertia along the x-axis.

The algorithm involves a several steps. For particles that possess no symmetries, one step can be skipped. The algorithm operates on a coordinate grid and consists of the following steps:

1. First, the particle mass center coordinate $\bar{r}$ is calculated, according to

$$\bar{r} = \sum_{i=1}^{N} m_i r_i, \tag{A1}$$

   where r_i is (3x1) column vector describing the coordinate of the grid point with index i, and m_i is the mass of the corresponding dipole. The dipole grid is then displaced so that the mass center is located at the origin.

2. Next, the inertia matrix I relative to the origin is calculated using

$$I = -\sum_{i=1}^{N} m_i [R]_i^2, \tag{A2}$$

   where $[R]_i$ is the skew-symmetric matrix associated with coordinate r, defined as

$$[R] = \begin{pmatrix} 0 & -z & \boxtimes \\ z & 0 & -x \\ -\boxtimes & x & 0 \end{pmatrix}. \tag{A3}$$

   I contains the products of inertia along the Cartesian coordinate axes, i.e.

$$I = \begin{pmatrix} I_{xx} & I_{xy} & I_{xz} \\ I_{xy} & I_{yy} & I_{yz} \\ I_{xz} & I_{yz} & I_{zz} \end{pmatrix}. \tag{A4}$$

   Since I is real and symmetric, it can be diagonalized using eigenvector decomposition, as

$$\Lambda = Q I Q^T, \tag{A5}$$

where Λ is a diagonal matrix with elements I_1, I_2 and I_3, which are called the principal moments of inertia. The diago-
nalization is performed in such way that $I_1 \leq I_2 \leq I_3$. The columns of Q, Q_1, Q_2 and Q_3, are the corresponding principal
axes.

It follows that Q is a rotation matrix, which rotates the x, ⊠ and z-axes to corresponding axes of inertia. Thus, to align
the particle principal axes to the coordinate axes, one has to rotate the particle grid by the inverse of Q, i.e. Q^T. In order
to ensure that the rotation does not mirror the particle (that the rotation is pure), one has to make sure that $\det\left(Q^T\right) = 1$.
The rotation matrix A is thus calculated as

$$A = \frac{Q^T}{|Q^T|}. \tag{A6}$$

After the rotation, recalculation of the inertia matrix should yield

$$I = \begin{pmatrix} I_{xx} & 0 & 0 \\ 0 & I_{yy} & 0 \\ 0 & 0 & I_{zz} \end{pmatrix}, \tag{A7}$$

With

$$I_{xx} \leq I_{yy} \leq I_{zz}. \tag{A8}$$

This criteria must always be satisfied, i.e. any of the remaining steps must make sure that it does not violate the condition.

3. If the particle contains symmetries, then two or all of the principal moments of inertia can be equal. This means that
   the rotation in the previous step is unambiguous, i.e. several possible orientations fulfill Eq. A8. As an example, for
   hexagonal plates, $I_{xx} = I_{yy}$, meaning that its orientation in the xy-plane is unambiguous. It is desirable to remove this
   uncertainty, which here is done by minimizing the particle dimensions along the coordinate axes. Three cases are possible
   and are treated as follows:

   – $I_{xx} = I_{yy} = I_{zz}$: The particle is spherically symmetric (for example, a six bullet rosette), hence no rotation will have
     an impact on I. First, the particle dimension along the z-axis is minimized by rotation around the x and y-axis.
     Similarly, the particle dimension along the x-axis is then maximized by rotation around the z-axis.

   – $I_{yy} = I_{zz}$: The particle is symmetric around the x-axis (a hexagonal column for example). The particle dimension
     along the z-axis is minimized by rotation around the x-axis.

   – $I_{yy} = I_{xx}$: The particle is symmetric around the z-axis (for example, a hexagonal plate). The particle dimension
     along the x-axis is maximized by rotation around the z-axis

4. In the final step, it is determined whether the particle is aligned upside down or upright. First, the minimum circumsphere
   of the particle is calculated, with its corresponding center. If the center is found to be below the mass-center of the particle
   (with respect to the z-axis), then the particle is said to be aligned upright. Vice versa, it is said to be aligned upside down
   in the case when the sphere center is above the mass center. In this case, the particle is rotated 180° around the x-axis to
   be upright.
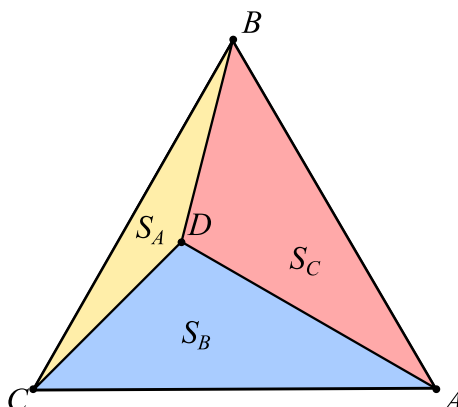
Figure B1. Geometry of triangular barycentric interpolation.

Appendix B: Barycentric interpolation

605   On a icosahedral grid any arbitrary point on the sphere is accompanied by three nearest points that form a equilateral triangle. Within this triangle the value at that point can be interpolated from the vertices of the triangle. A schematic of the problem is shown in Fig. B1. The vertices A, B, and C form the equilateral triangle ABC. The point D is the evaluation point. Always two vertices and the evaluation point D form a sub-triangle. For example, the vertices B and C and the evaluation D form the triangle BCD on the opposing side of vertex A. The idea behind the barycentric interpolation is to use the ratio of the area of a

610   sub-triangle and the area of the triangle ABC as interpolation weights. The weight belonging to vertex A is

$$w_A = \frac{S_A}{S_{ABC}} \tag{B1}$$

with S_A the area of sub-triangle BCD and S_{ABC} the area of the triangle ABC. The weights belonging to the other two vertices are analogue to the weight of vertex A. The area S of a triangle is using Heron's formula

$$S_i = \sqrt{s(s-u)(s-\boxtimes)(s-w)} \tag{B2}$$

615   with

$$s = \frac{u + \boxtimes + w}{2} \tag{B3}$$

and $u, \boxtimes, w$ the sides of the triangle i. The interpolated value f_{int} at the evaluation point D is

$$f_{int}(D) = w_A f(A) + w_B f(B) + w_C f(C) \tag{B4}$$

with $f(i)$ the value at a vertex i.

620 **Appendix C: Spherical harmonics expansion of the Mueller and scattering matrix elements**

Each matrix element $X_{ij}(\theta_{inc}, \phi_{inc}, \theta_s, \phi_s)$ of the Mueller matrix or the scattering matrix is expanded in a spherical harmonics series over the scattering directions (θ_s, ϕ_s).

$$X_{ij}(\theta_{inc}, \phi_{inc}, \theta_s, \phi_s) = \sum_{l=0}^{l_{max}} \sum_{m=-l}^{l} C_{lm}(\theta_{inc}, \phi_{inc}) Y_{lm}(\theta_s, \phi_s) \tag{C1}$$

with Y_{lm} the spherical harmonic function of the l-th and m-th order and with

625 $$C_{lm}(\theta_{inc}, \phi_{inc}) = \int_{\Omega_s} X_{ij}(\theta_{inc}, \phi_{inc}, \theta_s, \phi_s) Y_{lm}^*(\theta_s, \phi_s) d\Omega_s \tag{C2}$$

the expansion coefficients of the incidence direction $(\theta_{inc}, \phi_{inc})$. To save data space, the expansion of X_{ij} is truncated to the value l_{max}. l_{max} is defined as the lowest l for which holds, that

$$\left[\int_{\Omega_s} \left| X_{ij}(\theta_{inc}, \phi_{inc}, \theta_s, \phi_s) - \sum_{l=0}^{l_{max}} \sum_{m=-l}^{l} C_{lm}(\theta_{inc}, \phi_{inc}) Y_{lm}(\theta_s, \phi_s) \right|^2 d\Omega_s \right]^{\frac{1}{2}} < \varepsilon_{M11}. \tag{C3}$$

ε_{M11} is 0.5% of the standard deviation over the scattering directions (θ_s, ϕ_s) of the $X_{11}(\theta_{inc}, \phi_{inc})$ matrix element. For the actual 630 calculation of the spherical harmonics the SHTns library version 2.8 (Schaeffer, 2013) and its Python interface are used.

Appendix D: Rotation matrix elements

The rotation matrix elements R_{ij} are

$$R_{11} = \cos(\gamma)\cos(\beta)\cos(\alpha) - \sin(\gamma)\sin(\alpha) \tag{D1}$$

635 $$R_{12} = \cos(\gamma)\cos(\beta)\sin(\alpha) + \sin(\gamma)\cos(\alpha) \tag{D2}$$

$$R_{13} = -\cos(\gamma)\sin(\beta) \tag{D3}$$

$$R_{21} = -\sin(\gamma)\cos(\beta)\cos(\alpha) - \cos(\gamma)\sin(\alpha) \tag{D4}$$

640

$$R_{22} = -\sin(\gamma)\cos(\beta)\sin(\alpha) + \cos(\gamma)\cos(\alpha) \tag{D5}$$

$$R_{23} = \sin(\gamma)\sin(\beta) \tag{D6}$$

645 $$R_{31} = \sin(\beta)\cos(\alpha) \tag{D7}$$

$$R_{32} = \sin(\beta)\sin(\alpha) \tag{D8}$$

$$R_{33} = \cos(\beta) \tag{D9}$$

650   with Euler angles α, β, and γ (Tsang et al., 2000).

References

Adams, I. S. and Bettenhausen, M. H.: The scattering properties of horizontally aligned snow crystals and crystal approximations at millimeter wavelengths, Radio Science, 47, 2012.

Bergadá, M., Labriola, M., González, R., Palacios, M. A., Marote, D., Andrés, A., García, J. L., Pascuala, D. S., Ordóñez, L., Rodríguez, M., Ortín, M. T., Esteso, V., Martínez, J., and Klein, U.: The Ice Cloud Imager (ICI) preliminary design and performance, in: 2016 14th Specialist Meeting on Microwave Radiometry and Remote Sensing of the Environment (MicroRad), pp. 27–31, https://doi.org/10.1109/MICRORAD.2016.7530498, 2016.

Buehler, S. A., Jiménez, C., Evans, K. F., Eriksson, P., Rydberg, B., Heymsfield, A. J., Stubenrauch, C. J., Lohmann, U., Emde, C., John, V. O., and et al.: A concept for a satellite mission to measure cloud ice water path, ice particle size, and cloud altitude, Quarterly Journal of the Royal Meteorological Society, 133, 109–128, https://doi.org/10.1002/qj.143, 2007.

Buehler, S. A., Defer, E., Evans, F., Eliasson, S., Mendrok, J., Eriksson, P., Lee, C., Jiménez, C., Prigent, C., Crewell, S., and et al.: Observing ice clouds in the submillimeter spectral range: the CloudIce mission proposal for ESA's Earth Explorer 8, Atmos. Meas. Tech., 5, 1529–1549, https://doi.org/10.5194/amt-5-1529-2012, 2012.

Buehler, S. A., Mendrok, J., Eriksson, P., Perrin, A., Larsson, R., and Lemke, O.: ARTS, the Atmospheric Radiative Transfer Simulator – version 2.2, the planetary toolbox edition, Geoscientific Model Development, 11, 1537–1556, https://doi.org/10.5194/gmd-11-1537-2018, https://www.geosci-model-dev.net/11/1537/2018/, 2018.

Côté, J., Gravel, S., Méthot, A., Patoine, A., Roch, M., and Staniforth, A.: The Operational CMC-MRB Global Environmental Multiscale (GEM) Model. Part I: Design Considerations and Formulation, Monthly Weather Review, 126, 1373–1395, 1998.

Defer, E., Galligani, V. S., Prigent, C., and Jimenez, C.: First observations of polarized scattering over ice clouds at close-to-millimeter wavelengths (157?GHz) with MADRAS on board the Megha-Tropiques mission, Journal of Geophysical Research: Atmospheres, 119, 2014JD022 353, https://doi.org/10.1002/2014JD022353, 2014.

Ding, J., Bi, L., Yang, P., Kattawar, G. W., Weng, F., Liu, Q., and Greenwald, T.: Single-scattering properties of ice particles in the microwave regime: Temperature effect on the ice refractive index with implications in remote sensing, Journal of Quantitative Spectroscopy and Radiative Transfer, 190, 26–37, https://doi.org/10.1016/j.jqsrt.2016.11.026, http://www.sciencedirect.com/science/article/pii/S0022407316306367, 2017.

Draine, B. T. and Flatau, P. J.: Discrete-Dipole Approximation For Scattering Calculations, J. Opt. Soc. Am. A, 11, 1491–1499, https://doi.org/10.1364/JOSAA.11.001491, http://josaa.osa.org/abstract.cfm?URI=josaa-11-4-1491, 1994.

Emde, C.: A polarized discrete ordinate scattering model for simulations of limb and nadir long-wave measurements in 1-D/3-D spherical atmospheres, Journal of Geophysical Research, 109, https://doi.org/10.1029/2004jd005140, 2004.

Eriksson, P., Buehler, S., Davis, C., Emde, C., and Lemke, O.: ARTS, the atmospheric radiative transfer simulator, version 2, Journal of Quantitative Spectroscopy and Radiative Transfer, 112, 1551–1558, https://doi.org/10.1016/j.jqsrt.2011.03.001, 2011.

Eriksson, P., Ekelund, R., Mendrok, J., Brath, M., Lemke, O., and Buehler, S. A.: A general database of hydrometeor single scattering properties at microwave and sub-millimetre wavelengths, Earth System Science Data, 10, 1301–1326, https://doi.org/10.5194/essd-10-1301-2018, https://www.earth-syst-sci-data.net/10/1301/2018/, 2018.

Eriksson, P., Rydberg, B., Mattioli, V., Thoss, A., Accadia, C., Klein, U., and Buehler, S. A.: Towards an operational Ice Cloud Imager (ICI) retrieval product, Atmospheric Measurement Techniques Discussions, 2019, 1–30, https://doi.org/10.5194/amt-2019-312, https://www.atmos-meas-tech-discuss.net/amt-2019-312/, 2019.

Gong, J. and Wu, D. L.: Microphysical properties of frozen particles inferred from Global Precipitation Measurement (GPM) Microwave Imager (GMI) polarimetric measurements, Atmospheric Chemistry and Physics, 17, 2741–2757, 2017.

Hong, G., Yang, P., Baum, B. A., Heymsfield, A. J., Weng, F., Liu, Q., Heygster, G., and Buehler, S. A.: Scattering database in the millimeter and submillimeter wave range of 100–1000 GHz for nonspherical ice particles, Journal of Geophysical Research: Atmospheres (1984–2012), 114, 2009.

Hou, A. Y., Kakar, R. K., Neeck, S., Azarbarzin, A. A., Kummerow, C. D., Kojima, M., Oki, R., Nakamura, K., and Iguchi, T.: The Global Precipitation Measurement Mission, Bulletin of the American Meteorological Society, 95, 701–722, https://doi.org/10.1175/BAMS-D-13-00164.1, 2013.

Liu, G.: A database of microwave single-scattering properties for nonspherical ice particles, Bulletin of the American Meteorological Society, 89, 1563–1570, https://doi.org/10.1175/2008BAMS2486.1, 2008.

Lu, Y., Jiang, Z., Aydin, K., Verlinde, J., Clothiaux, E. E., and Botta, G.: A polarimetric scattering database for non-spherical ice particles at microwave wavelengths, Atmospheric Measurement Techniques, 9, 5119–5134, 2016.

Mätzler, C.: Thermal microwave radiation: applications for remote sensing, vol. 52, Iet, 2006.

Milbrandt, J. A. and Yau, M. K.: A Multimoment Bulk Microphysics Parameterization. Part I: Analysis of the Role of the Spectral Shape Parameter, Journal of the Atmospheric Sciences, 62, 3051–3064, https://doi.org/10.1175/JAS3534.1, 2005a.

Milbrandt, J. A. and Yau, M. K.: A Multimoment Bulk Microphysics Parameterization. Part II: A Proposed Three-Moment Closure and Scheme Description, Journal of the Atmospheric Sciences, 62, 3065–3081, https://doi.org/10.1175/JAS3535.1, 2005b.

Mishchenko, M. I., Hovenier, J. W., and Travis, L. D., eds.: Light scattering by nonspherical particles, Academic Press, 2000.

Mishchenko, M. I., Travis, L. D., and Lacis, A. A.: Scattering, absorption, and emission of light by small particles, Cambridge university press, 2002.

Mlawer, E. J., Payne, V. H., Moncet, J.-L., Delamere, J. S., Alvarado, M. J., and Tobin, D. C.: Development and recent evaluation of the MT_CKD model of continuum absorption, Philosophical Transactions of the Royal Society A: Mathematical, Physical and Engineering Sciences, 370, 2520–2556, 2012.

Prigent, C., Aires, F., Wang, D., Fox, S., and Harlow, C.: Sea-surface emissivity parametrization from microwaves to millimetre waves, Quarterly Journal of the Royal Meteorological Society, 143, 596–605, https://doi.org/10.1002/qj.2953, 2017.

Rosenkranz, P. W.: Water vapor microwave continuum absorption: A comparison of measurements and models, Radio Science, 33, 919–928, https://doi.org/10.1029/98RS01182, 1998.

Rothman, L., Gordon, I., Babikov, Y., Barbe, A., Chris Benner, D., Bernath, P., Birk, M., Bizzocchi, L., Boudon, V., Brown, L., and et al.: The HITRAN2012 molecular spectroscopic database, Journal of Quantitative Spectroscopy and Radiative Transfer, 130, 4–50, https://doi.org/10.1016/j.jqsrt.2013.07.002, 2013.

Satoh, M.: Icosahedral grids, Springer Praxis Books, Springer Berlin Heidelberg, 2014.

Schaeffer, N.: Efficient spherical harmonic transforms aimed at pseudospectral numerical simulations, Geochemistry, Geophysics, Geosystems, 14, 751–758, https://doi.org/10.1002/ggge.20071, 2013.

Tretyakov, M. Y., Koshelev, M. A., Dorovskikh, V. V., Makarov, D. S., and Rosenkranz, P. W.: 60-GHz oxygen band: precise broadening and central frequencies of fine-structure lines, absolute absorption profile at atmospheric pressure, and revision of mixing coefficients, Journal of Molecular Spectroscopy, 231, 1–14, https://doi.org/10.1016/j.jms.2004.11.011, http://www.sciencedirect.com/science/article/pii/S0022285204003650, 2005.

Tsang, L., Kong, J. A., and Ding, K.-H.: Scattering of Electromagnetic Waves, Theories and Applications, vol. 27, John Wiley & Sons, 2000.

Yurkin, M. A. and Hoekstra, A. G.: The discrete-dipole-approximation code ADDA: Capabilities and known limitations, Journal of Quantitative Spectroscopy and Radiative Transfer, 112, 2234–2247, https://doi.org/10.1016/j.jqsrt.2011.01.031, http://www.sciencedirect.com/science/article/pii/S0022407311000562, 2011.

Zeng, X., Skofronick-Jackson, G., Tian, L., Emory, A. E., Olson, W. S., and Kroodsma, R. A.: Analysis of the Global Microwave Polarization Data of Clouds, Journal of Climate, 32, 3–13, https://doi.org/10.1175/JCLI-D-18-0293.1, 2019.

730